A-CARE Project

Final Report

Silke Groß[1)], Bernadett Weinzierl[2)], Maximilian Dollner[2)], Moritz Haarig[3)], Ulla Wandinger[3)], Athena Floutsi[3)], Eleni Marinou[4)], Vassilis Amiridis[4)], Florian Ewald[1)], Anna Gialitaki[4)]

[1)]Deutsches Zentrum für Luft- und Raumfahrt, Institut für Physik der Atmosphäre, Germany
[2)]Universität Wien, Austria
[3)]Leibniz Institute for Tropospheric Research, Germany
[4)]National Observatory of Athens, Greece

ESA Contract No. 4000125810/NL/CT/gp

Earthcare Pre-Launch Campaigns Activity:

A-CARE

Content

1 ACRONYMS & ABBREVIATIONS

AERONET	Aerosol Robotic Network
A-LIFE	Absorbing aerosol layers in a changing climate: aging, lifetime and dynamics
AOD	Aerosol Optical Depth
ATLID	Atmospheric Lidar
CALIPSO	Cloud-Aerosol Lidar with Orthogonal Polarization
CAPTIVATE	Cloud, Aerosol and precipitation from multiple Instruments using a Variational TEchnique
CNR-IMAA	CNR – Istituto di Metedologie per l'Analisi Ambientale Indirizzo
CPR	Cloud Profiling Radar
CyCARE	Cyprus Clouds Aerosol and Rain Experiment
DAR	Data Acquisition Report
DARDAR	raDAR/liDAR
DORSY	Doppler Radar and Synergy Products for EarthCARE
DREAM-NMM	Dust Regional Atmospheric Model – Non-hydtrostatic Multiscale Model
EARLINET	European Aerosol Lidar Network
EarthCARE	Earth Clouds, Aerosol and Radiation Explorer
ESA	European Space Agency
FLEXPART	Flexiple Particle dispersion model
FMI	Finnish Meteorological Insitute
GFS	Global Forecast System
HETEAC	Hybrid End-To-End Aerosol Classification
INOE	National Institute for Research and Development for Optoelectronics
IWC	Ice Water Content
LACROS	Leipzig Aerosol and Cloud Remote Observations System
NCEP	National Center for Environmental Prediction
NOA	National Observatory of Athens
PLDR	Particle Linear Depolarization Ratio
TROPOS	Institute of Tropospheric Physics Leipzig
SoW	Statement of Work
VarCloud	variational radar-lidar ice cloud retrieval algorithm
WRF-ARW	Weather Research and Forcasting Model – Advanced Research WRF

1. INTRODUCTION / OVERVIEW

This document describes the work performed in the frame of the EarthCARE preparation campaign (A-CARE). It covers the tasks in response to the Statement of Work (SoW) from ESA (EOP-SM/3114/DS-ds of 30 October 2017). The description of the aircraft data and their analysis used in this activity are described in the DAR (Data Acquisition Report) which is given in annex I.

The main scientific objectives of A-CARE are derived from the scientific objectives of EarthCARE. The EarthCARE mission will advance our understanding of the role that clouds and aerosols play in reflecting incident solar radiation back into space and trapping infrared radiation emitted from Earth's surface by providing vertical cloud and aerosol profile information in connection with collocated broadband solar and thermal radiance measurements (Illingworth et al. 2015).
In the context of general ESA campaign objectives, A-CARE addresses directly the programmatic needs of EarthCARE Mission Development, particularly relating to the development and refinement of Geophysical Product Algorithms.

The main objectives of A-CARE project are as follows:

i. to acquire and process high quality airborne in-situ datasets for microphysical particle characteristics in conjunction with extended correlative data
ii. to perform initial analyses of data quality and generate first estimates for the EarthCARE aerosol-cloud discrimination and classification schemes
iii. to deliver a set of products available for EarthCARE validation as demonstration for planned EarthCARE cal/val activities.

EarthCARE aims at improving our understanding of aerosol/cloud interactions on the global scale by providing accurate vertical distributions of key aerosol and cloud properties, in order to assess their impact on the Earth's radiative budget and climate. Optical properties needed for radiative-transfer calculations are mainly related to the particle load and its vertical distribution (extinction coefficient) as well as the particle type (indicative of radiative properties as single-scattering albedo, asymmetry parameter, extinction spectral dependencies). In order to retrieve the required information from EarthCARE observations, the Hybrid End-To-End Aerosol Classification (HETEAC) model is being developed for common use in the Level 2 (L2) algorithms. It will allow aerosol typing based on measurements of extinction coefficient, lidar ratio and particle linear depolarization ratio at 355 nm with ATLID and provides related radiative properties of the detected aerosol types for radiative-transfer models and closure studies. This novel approach necessitates highly reliable input, from both the instrument and the underlying aerosol model, and thus requires extensive verification and validation efforts under various atmospheric conditions.

Measurements performed during A-LIFE, CyCARE and PRE-TECT provide a unique opportunity to support the EarthCARE developments. The Eastern Mediterranean is an optimum testbed for investigating atmospheric mixtures of dust, pollution, smoke, and marine particles. Moreover, because of the enhanced ice-nucleating ability of mineral dust particles, ice formation often occurs in the aerosol layers.

To achieve these above-mentioned objectives the following work has been performed:

- Design, plan and conduct a research flights within the to the existing A-LIFE experiment.
- Perform continuous ground-based remote sensing measurements at Limassol and Finokalia
- Derive the optical profiles from lidar measurements and select the layers corresponding to the airborne observations
- Apply the optimal estimation technique to derive the best mixture of basic aerosol components
- Use the prescribed microphysical properties of aerosol components to calculate size distributions and effective radii of the complex aerosol mixture and compare these quantities to the airborne in-situ measurements

2. A-CARE PROJECT AND DATA

2.1 A-LIFE / A-CARE

2.2 Ground-based measurement

2.2.1 Limassol /TROPOS

The Leipzig Aerosol and Cloud Remote Observations System (LACROS) is operating on the premises of the Cyprus University of Technology from October 2016 until March 2018. LACROS is composed of different remote-sensing instruments. A Raman polarization lidar of type PollyXT (Engelmann et al, AMT 2016) emits a laser pulses in order to study the vertical profile of aerosol properties. The backscatter coefficient is measured at 355, 532 and 1064 nm, the extinction coefficient (Raman method) and the depolarization ratio at 355 and 532 nm. This configuration is ideally suited to test future EarthCARE algorithms as it operates at the same wavelength (355 nm). Additionally, a comparison with CALIPSO products is possible (532 and 1064 nm).

A 35-GHz cloud radar is used to study cloud properties using microwave radiation. Different other measurement systems are deployed to measure the properties of the precipitation on ground (disdrometer), aerosol and cloud dynamics (Doppler lidar) and water vapor and liquid water path (microwave radiometer). An overview about the station and its instruments is given in Fig. 1.

Figure 1 The measurement systems of LACROS. Different measurement systems are used to measure aerosol (Raman lidar), cloud particles (cloud radar), air motions (Doppler lidar), rain (disdrometer) and water vapor (microwave radiometer).

2.2.2 Finokalia

The A-life experiment was clustered with the Pre-TECT experiment of the National Observatory of Athens (NOA). Pre-TECT location was on the North coast of Crete, at the Finokalia ACTRIS station (35.34∘ N, 25.67∘ E; 193m asl). The Instrumentation deployed in Pre-TECT consist of the PollyXT lidar system of NOA (Engelmann et al, AMT 2016; similar lidar as the one described from TROPOS above) part of the EARLINET network, a CIMEL sun-photometer part of the AERONET network, a 35-GHz cloud radar from CNR-IMAA, and other auxiliary instruments (e.g. microwave radiometer from INOE, Doppler lidar from FMI). An overview of the station and its instruments is given in Fig. 2 and all the measurement quicklooks can be found in .

During daytime, due to strong background radiation, the use of only PollyXT elastic backscattering channels is imposed and the particle backscatter coefficient can be determined at 355, 532 and 1064 nm, the particle linear depolarization ratio (PLDR) at 355 and 532 nm and the Angstrom exponent at 355/532 and 532/1064 nm. During nighttime operation, the available Raman channels allow for determination of particle extinction coefficient, the particle lidar ratio (LR) at 355 and 532 nm and the water vapour mixing ratio. PollyXT employs two different telescopes for aerosol profiling and characterization in the far-range (i.e. > 800 m above the ground, up to 15-16km) and near-range (> 200m above the ground up to 2-2.5km). The near-range channels are only available for the 355, 378, 532 and 607 nm.

AERONET products from the CIMEL sun-photometer were also used herein to provide information on the columnar aerosol properties by means of AOD (at 8 wavelengths; 340 – 1640nm) and sky radiance (at 4 wavelengths; 440, 670, 870 and 1020nm). The full set of these observations is used to derive the columnar particle size distribution, the complex spectral refractive index, the single scattering albedo and the phase function. For the purposes of this study, AODs were used to constrain the daytime lidar retrievals, while the derived columnar size distributions acted complementary to lidar profiles as indication on the aerosol types present.

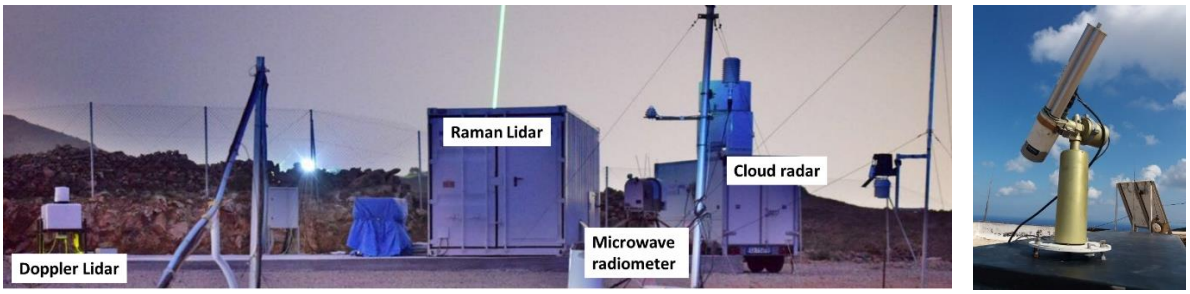

Figure 2 The Measurement systems of Pre-TECT experiment: PollyXT Raman Lidar, cloud radar, Doppler Lidar, microwave radiometer (left) and CIMEL sun-photometer (right), at the Finokalia Observatory.

2.3 Auxiliary data

2.3.1 Finokalia

We used atmospheric models to assist the interpretation of the ground-based and airborne measurements above Finokalia. Specifically, the DREAM-NMM dust model (Nickovic et al., 2001) and the FLEXPART Lagrangian model, driven by the forecasting fields of WRF-ARW at 12x12 km resolution (Stohl et al., 2005).

Dust forecasts are provided by DREAM-NMM model. Its meteorological core is the NCEP Nonhydrostatic Mesoscale Model on E-grid (NCEP/NMME) (Janjic et al., 2001). Surface properties are defined using the USGS global 1-km land cover data and the USDA global 1-km soil. The model is configured at 0.2°×0.2° resolution and includes 8 dust size bins with effective radii of 0.15, 0.25 0.45, 0.78, 1.3, 2.2, 3.8 and 7.1 μm. To generate the initial and boundary conditions of the simulations on a 0.5° by 0.5° latitude longitude grid, the NCEP Global Forecast System (GFS) analysis is used.

Source-receptor sensitivity study is carried out with the atmospheric dispersion FLEXPART-WRF model. FLEXPART ("FLEXible PARTicle dispersion model") is a Lagrangian transport and dispersion model suitable for the simulation of a large range of atmospheric transport processes. Apart from transport and turbulent diffusion, it is able to simulate dry and wet deposition, decay, linear chemistry; It is used to simulate air parcel trajectories and particle positions in backward mode (48 hours) driven by the hourly WRF-ARW forecasting fields at 12×12 km resolution. A total of 10000 tracer particles were released at different heights over the Finokalia station, to complement the characterization of the examined aerosol layers presented herein.

3. DATA PROCESSING AND STRUCTURE

3.1 Airborne data

The description of the data, information on data quality and processing, system calibration, as well as on data products can be found in the Data Acquisition Report in Annex I (DAR).

3.2 Ground-based data

A short overview about the ground-based lidar measurements will be provided. The cases were carefully selected in close cooperation with the airborne in situ measurements to cover various aerosol scenarios. In this section the time-height displays of the signal are shown to

characterized the scene. The profiles measured by the lidar provide the optical properties for the next steps. The lidar ratio and the particle linear depolarization ratio are the key parameters for the aerosol type separation. At daytime, the sky background often hampers a so-called Raman evaluation of the lidar data to provide the extinction coefficient independently and to derive the extinction-to-backscatter ratio (lidar ratio). In these cases, the lidar ratio was derived with the closest night-time observation in the same aerosol layer. This lidar ratio was then used to analyse the lidar data recorded simultaneously to the Falcon flights.

Case 1 & 2 Saharan and Arabian Dust – 6 April 2017 – Cyprus

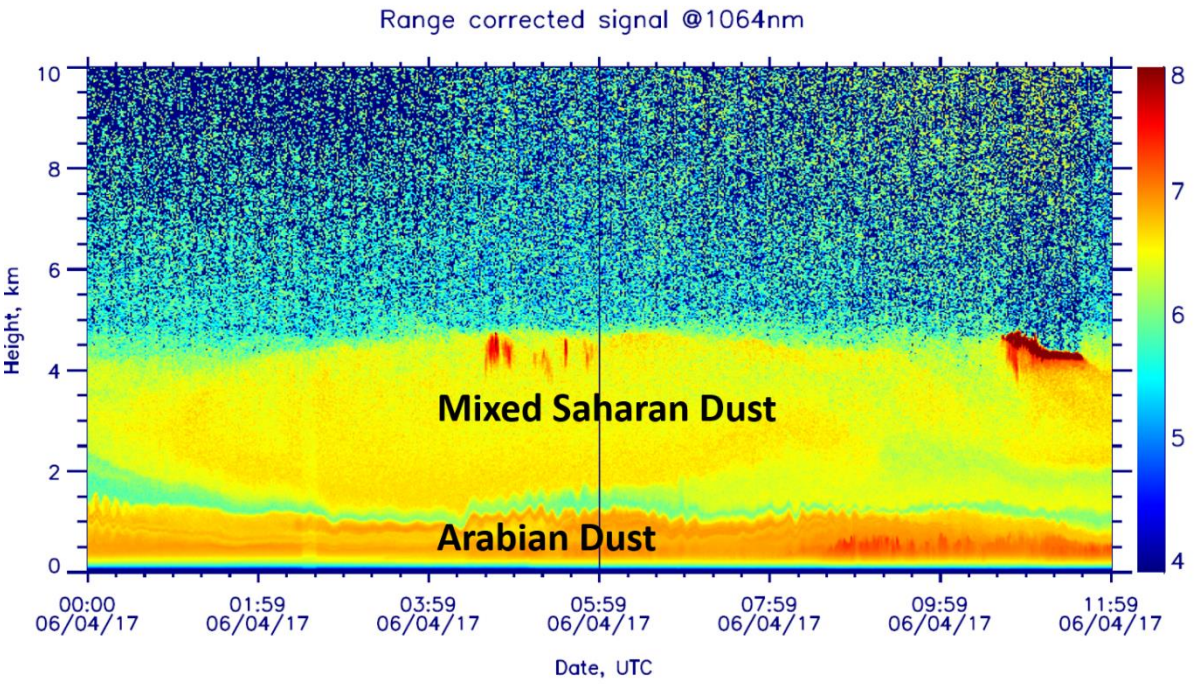

Figure 3 6 April 2017 (Cyprus)**:** Time-height display of the 1064 nm range corrected signal. A layer of mixed Saharan dust was observed on top of an Arabian dust layer. Falcon measurements at 06:00 - 08:00 UTC were used. Night-time Raman lidar measurements (00:00 - 03:00 UTC) were used to derive the lidar ratio used for simultaneous observations to Falcon aircraft.

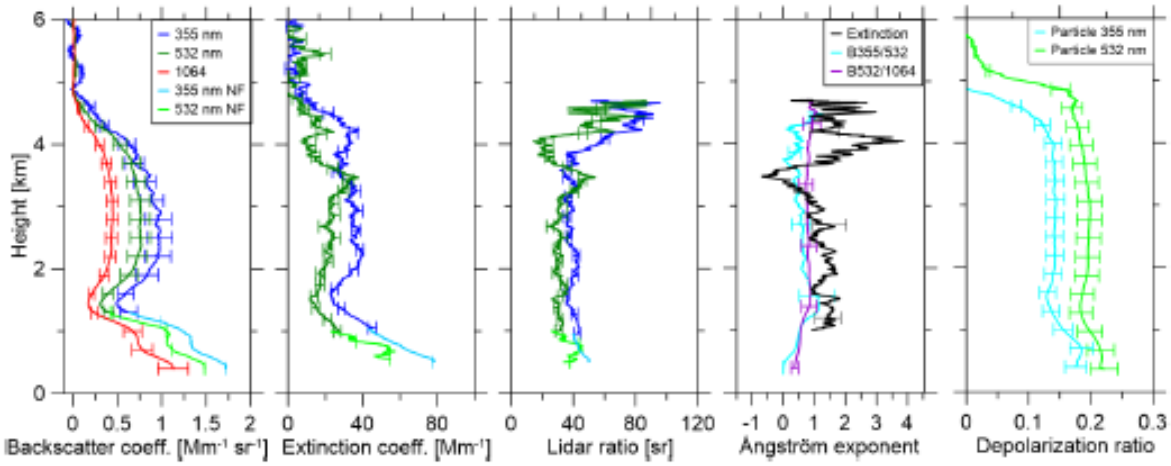

Figure 4 Optical properties measured with lidar on 6 April 2017, 00:00 - 03:00 UTC: Backscatter coefficient, extinction coefficient, lidar ratio (used for simultaneous observations to Falcon aircraft), Ångström exponent, particle linear depolarization ratio.

Case 3 Pollution – 11 April 2017 – Cyprus

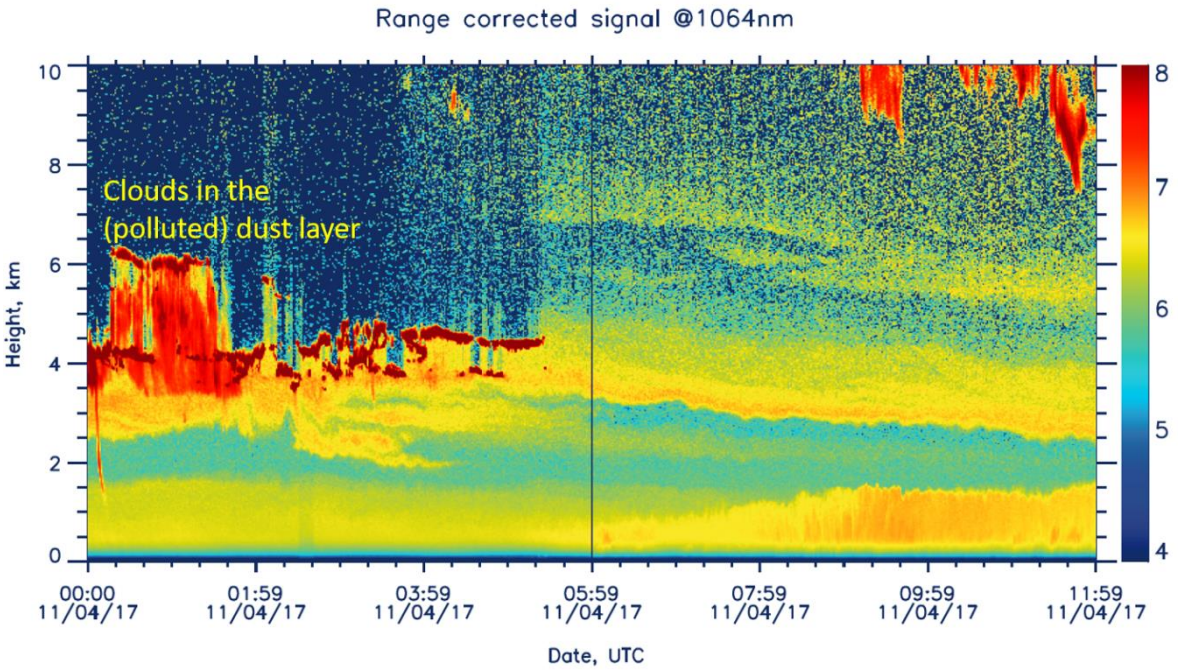

Figure 5 11 April 2017 (Cyprus)**:** Time-height display of the 1064 nm range corrected signal. A polluted dust layer was observed at 3 – 4 km height. For the comparison the pollution layer below 1.5 km height was used. Falcon measurements at 05:00 UTC were used.

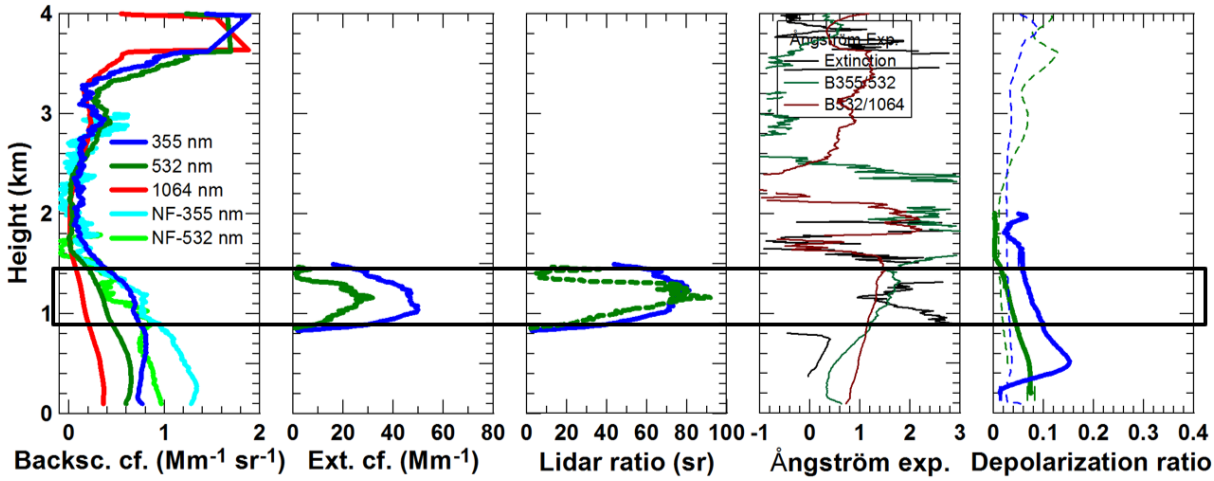

Figure 6 Optical properties measured with lidar on 11 April 2017, 04:30 - 06:00 UTC. The layer between 0.9 and 1.6 km was used for comparison with Falcon.

Case 4 Dust and Pollution – 14 April 2017 – Crete

The temporal development of the attenuated backscatter coefficient and the volume linear depolarization ratio on 13 and 14 April 2017 is shown in Fig. 7. Multiple low-depolarizing aerosol layers are observed up to 4 km, with low extinction coefficient values (< 30 Mm^{-1} at 355 nm) while significantly higher extinction coefficient values are observed below 2 km inside the boundary layer. The lidar-derived profiles are shown in Fig. 8. In order to derive the appropriate lidar ratio values needed for the daytime inversions collocated with the Falcon overpass, we used the closest nighttime lidar measurements. Good homogeneity of the scene between the night and daytime retrievals (marked by the purple rectangles on the attenuated backscatter coefficient time-height plot) supports this kind of analysis. A-Life collected measurements at 0.6, 2.2 and 2.5 km a.s.l. between 07:07 to 07:46 UTC (marked by the red rectangles in Fig. 7b).

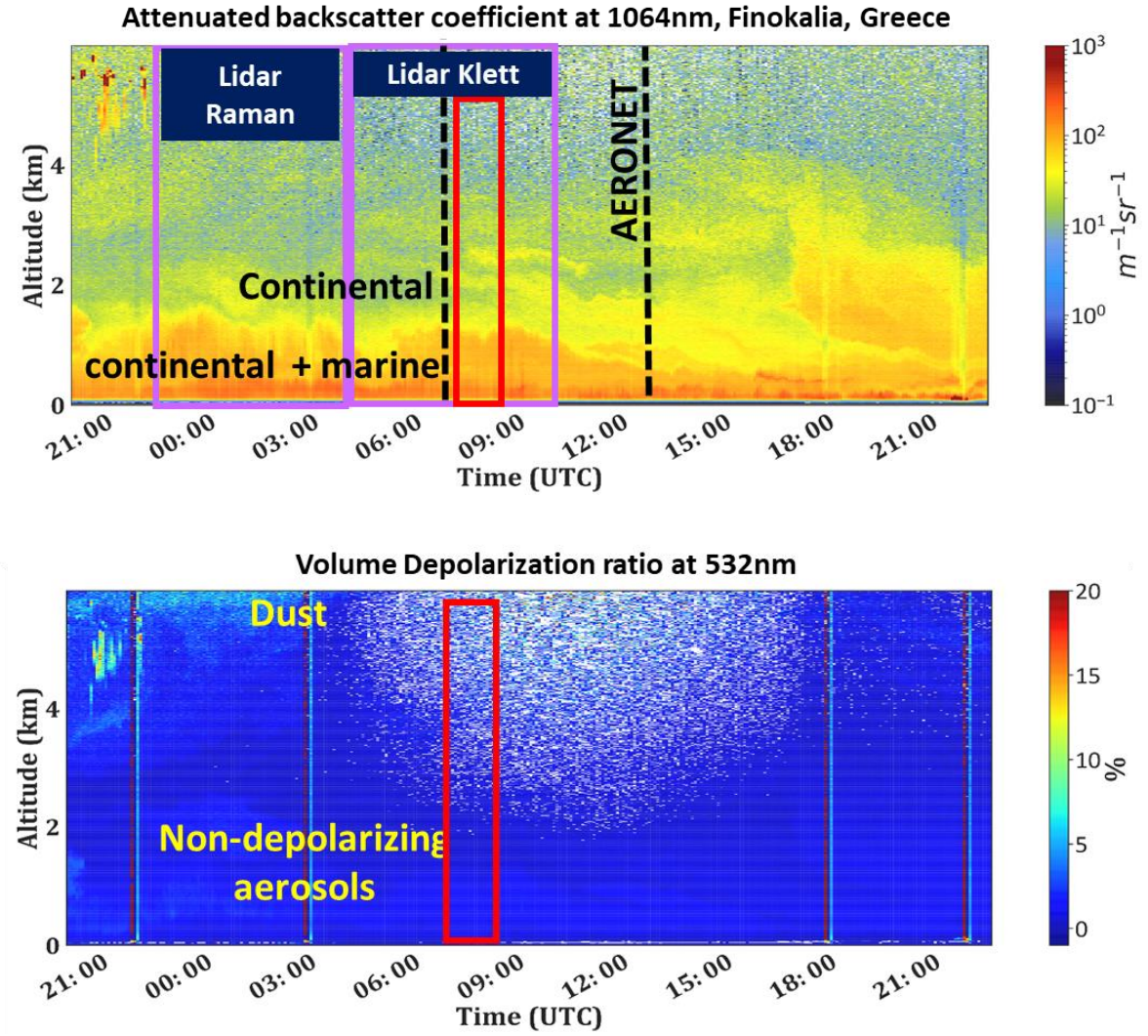

Figure 7 13 to 14 April 2017 (Crete): Time-height display of the 1064nm total attenuated backscatter coefficient (up) and the 532nm volume linear depolarization ratio (down). Night-time Raman measurements averaged between 13 April 2017, 22:00 UTC and 14 April 2017, 04:00 UTC were used to derive the lidar ratio values needed for the daytime inversions during the Falcon overflight (14 April 2017, 04:00 - 10:00 UTC). Red box: the time period that Falcon overpass Crete.

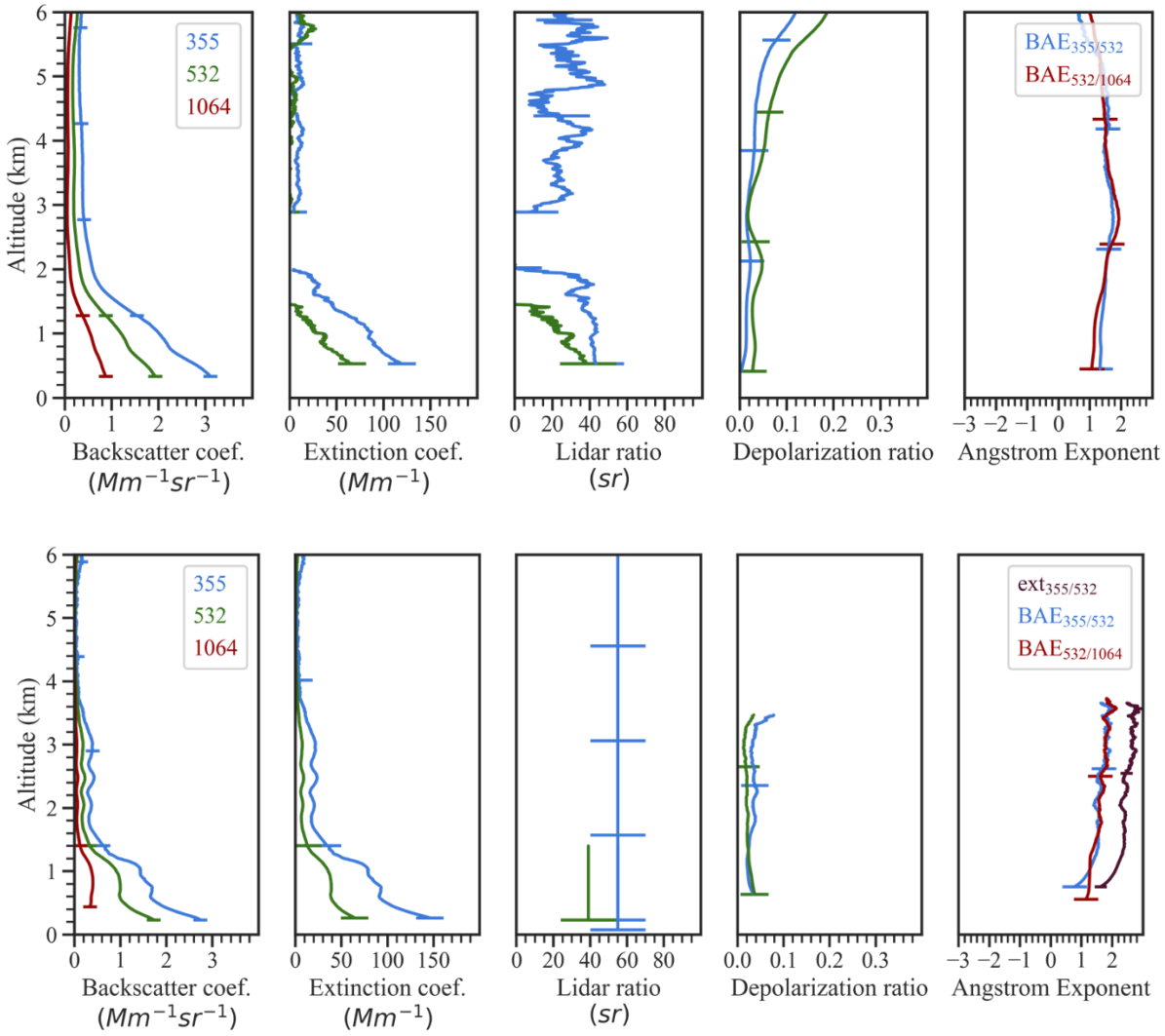

Figure 8 Optical properties measured with lidar on 13 April 2017, 22:00 UTC – 14 April, 04:00 UTC (up) and 14 April 2017, 4:00 - 10:00 UTC (down). The upper panel displays the night-time retrievals of the backscatter and extinction coefficient, lidar ratio, particle linear depolarization ratio and Angstrom exponent. An 680 m vertical smoothing was applied to all optical properties in order to filter out unwanted noise. Lower panel displays the day-time, Falcon collocated, retrievals of the backscatter and extinction coefficient, the particle linear depolarization ratio and the Angstrom exponent. Smoothing window here is 158 m.

Raman retrievals were carried out in order to derive the lidar ratio values needed to perform the Klett analysis for the time intervals collocated with the Falcon overflights on 14 April 2017. The layer-mean intensive optical properties between 0.5 – 1 km during the night-time and between 0.5 – 1 km and 1.9 – 3.5 km during the Falcon flights are provided in Table 1. For the Klett retrievals during the daytime overpass, the LRs derived in the previous night are used. The overall uncertainty of the assumed lidar ratio is estimated to be 40% (Ansmann et al., 1992; Hänel et al., 2012). The uncertainties of the LR and depolarization layers means are provided through the Pollynet algorithm (using error propagation assuming a backscatter coefficient error of 10%). Additionally, for the depolarization layer means, the standard deviation of the values in the layer are included in the uncertainties.

Table 1. Lidar layer-mean intensive optical properties and their uncertainties at 355 and 532 nm in blue and green on 13 and 14 April 2017. The aerosol sources are provided in the Raman cases by the modeled sources (Fig. 9) and in the Klett cases by the Falcon typing (Fig. 11).

Date, Time	**Height (Aerosol sources)**	**Meathod**	**Dep. Ratio (%)**	**Lidar ratio (sr)**
14 April, 4:00 - 10:00 UTC	1.9 – 3.5 km ase (organic matter + sulfates + marine + dust)	Klett	3.2±0.7% 2.1±0.5%	55±22* 39±17*
13 April, 22:00 UTC – 14 April, 04:00 UTC	*0.65 – 1.25 km ase (pollution + continental + marine)*	Raman	1.2±0.5% 3.5±0.3%	55±2** 39±17
14 April, 4:00 - 10:00 UTC	*0.7 – 1.0 km ase (Sea salt + organic matter + sulfate)*	Klett	2.5±0.3% 3.1±0.5%	

*Uncertainties of 40% on the assumed LR values as described in the text.

**Calculated for the heights 0.65 – 1.9 km ase.

The aerosol sources of the lidar retrievals are estimated using auxiliary data, as discussed herein. Based on the meteorological analysis, the presence of a trough, with its axis above West Turkey, led to the prevailing North flow above Greece, that pushed away dust from the Island of Crete towards East (Fig. 9a, b). The source-receptor sensitivity study carried out with the atmospheric dispersion FLEXPART-WRF model, revealed that the air masses arriving at lower altitudes (at 600 m and 2 km) are dominated by a mixture of marine particles mostly from the Aegean and continental pollution from the Balkans (Fig. 9c, d).

Low dust concentration was detected above 2.5 km, causing an increase of the particle linear depolarization ratio at both wavelengths. Dominance of fine-mode particles in the atmospheric column is also evident from the sun-photometer size distributions (Fig. 10) before and after the Falcon overflight. Lower concentration of coarse mode aerosols (due to marine and dust particles) is also observed.

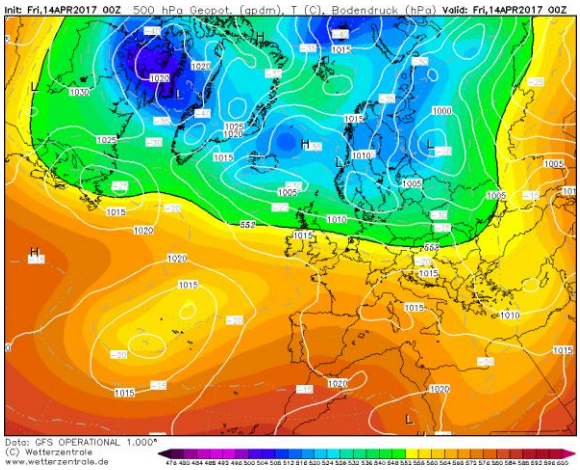

(a)

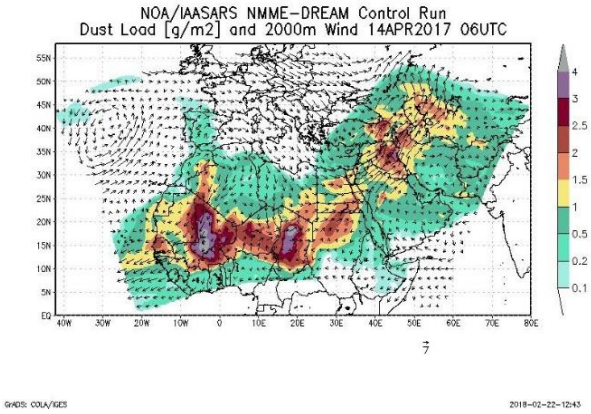

(b)

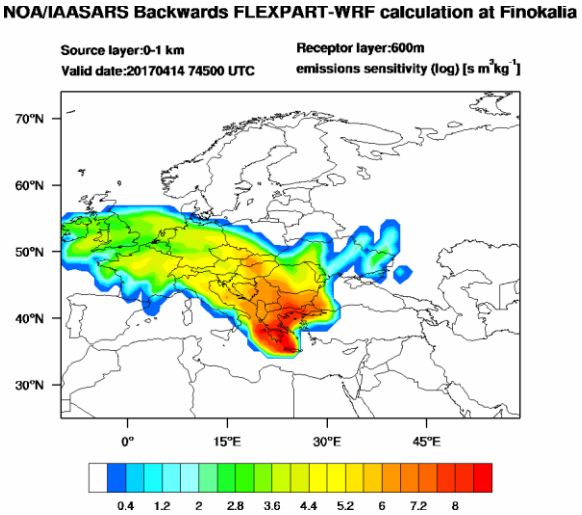

(c)

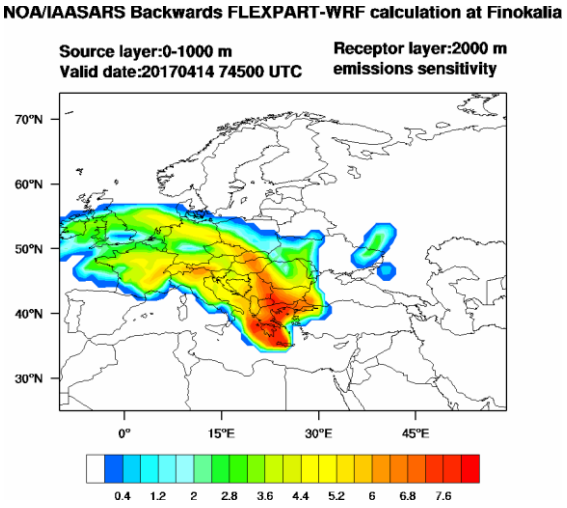

(d)

Figure 9 (a) Geopotential Height in 500hPa, along with isobars and surface isotherms on 14 April 00:00UTC (source: https://www.wetterzentrale.de/), (b) NMME-Dream Dust-load and wind direction at 2km height on 14 April 06:00 UTC, (c,d) Five-day backward FLEXPART-WRF calculation of emission sensitivity for the particles arriving at Finokalia on 14 April 2017 07:45 UTC, at heights 0.6 km (c) and 2 km (d) a.g.l., from source heights between 0 – 1 km a.g.l.

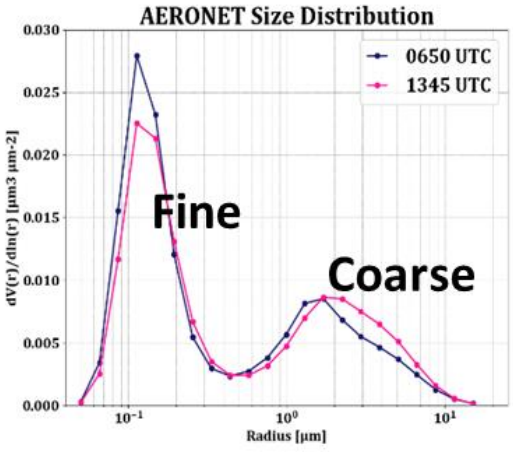

Figure 10 Volume size distribution derived from AERONET observations at Finokalia, on 14 April 2017 at 06:50 and 13:45 UTC. Fine mode particles prevail in the atmospheric column.

In the samples collected with the Falcon, mainly organic matter, sulfates, marine and low dust concentrations is found at 2.2 and 2.5 km samples (Fig. 11b, c). In the sample from 0.6 km, the aerosols are rich in sea-salt, organic matter and sulfates (Fig. 11a).

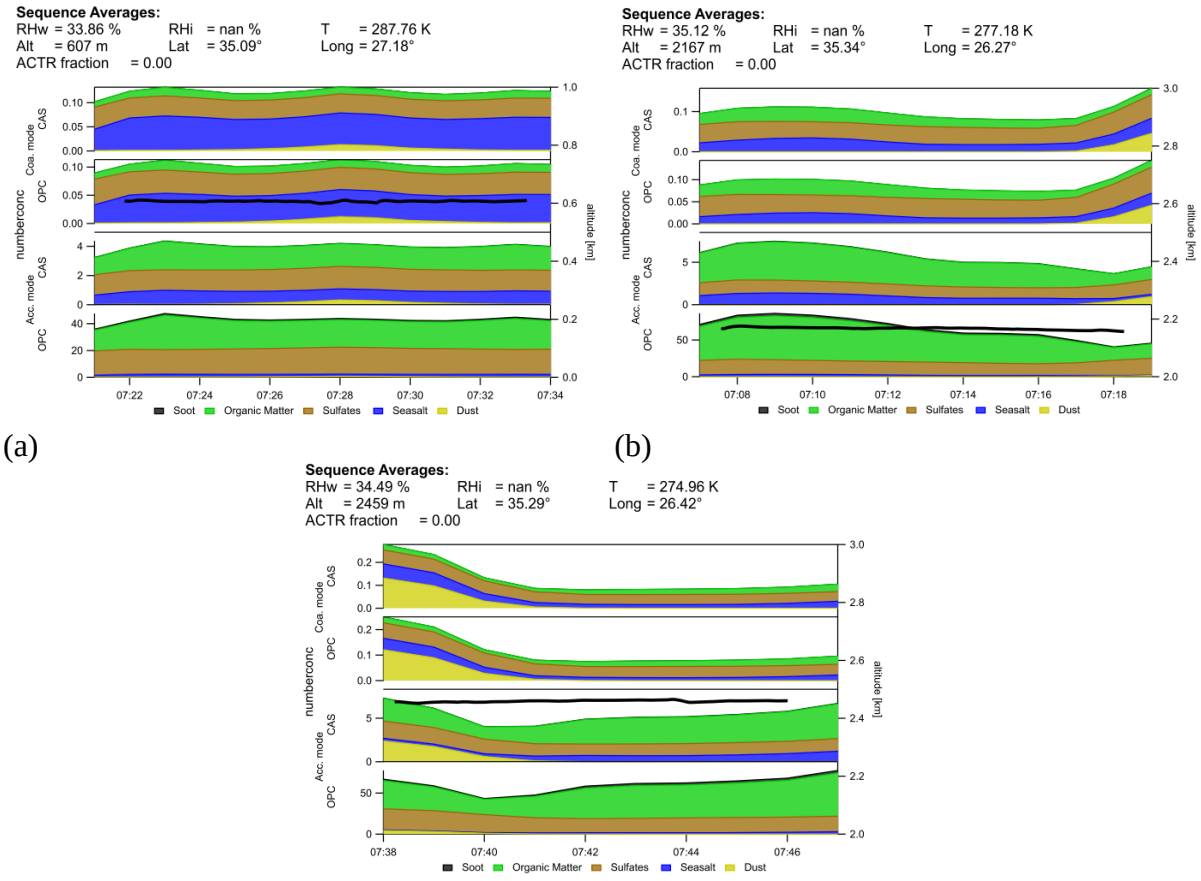

(a) (b)

(c)

Figure 11 Number concentrations of different particle types from in-situ samples on board Falcon at altitudes 0.6 (a), 2.2 (b) and 2.5 km (c) a.s.l.

Case 5 Marine and Pollution – 14 April 2017 – Cyprus

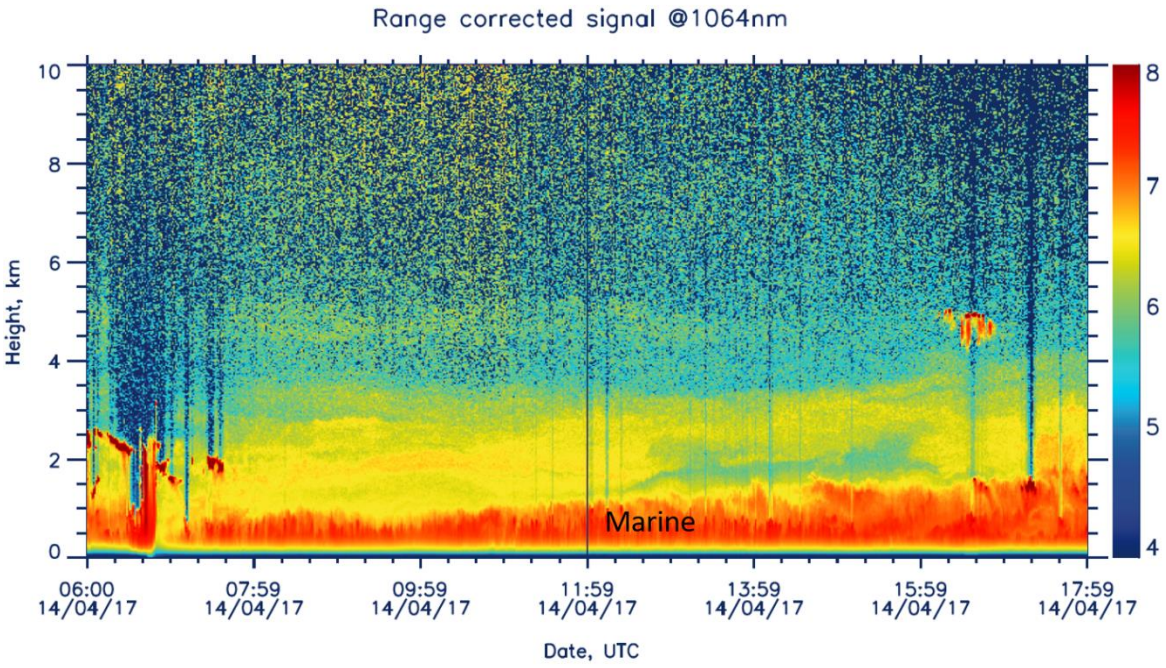

Figure 12 14 April 2017 (Cyprus)**:** Time-height display of the 1064 nm range corrected signal. A polluted dust layer was observed at 2– 3 km height. For the comparison the polluted marine layer below 1.0 km height was used. Falcon measurements at 12:19 – 12:29 UTC were used.

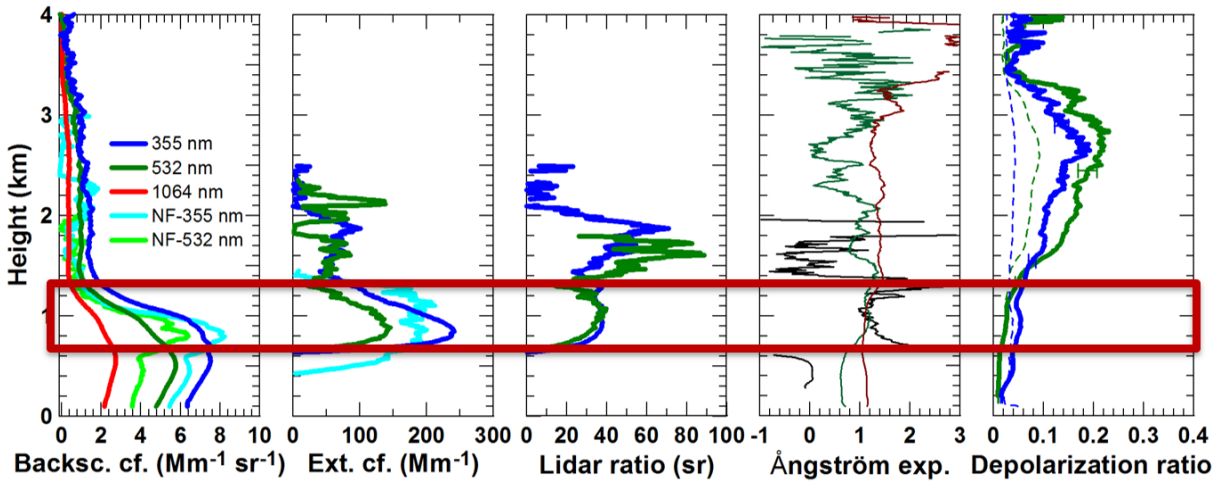

Figure 13 Optical properties measured with lidar on 14 April 2017, 12:00 - 13:30 UTC. The layer between 0.7 and 1.4 km was used for comparison with Falcon.

Case 6 Saharan Dust – 20 April 2017 – Crete

The temporal development of the attenuated backscatter coefficient and the volume linear depolarization ratio on 19 and 20 April 2017 is shown in Fig. 14. A strong dust outbreak is observed with dust particles reaching up to 6 km and ice and water clouds forming on top of the layers (dark red colors on attenuated backscatter coefficient plot). Raman measurements on 19 April 2017, were averaged between 18:00 and 19:20 UTC, in order to be used to derive the particle lidar ratio needed for the daytime retrievals on 20/4 (11:25 - 12:00 UTC) close in time to the Falcon overflight (12:16 – 13:19 UTC). Both measurements are conducted during the intense dust episode. However, from the attenuated backscatter plot (and the profiles of Fig. 15) we see slight difference in the intensity and vertical extend of the dust layer. Additionally, from the volume depolarization plot (and the particle depolarization plots in Fig. 15) we see that the aerosol depolarizing component is more dominant during the time of the Falcon overflight in comparison to the night-time retrieval. Specifically, the PLDR increases by 10% between night-time and day-time measurements, despite the fact that both observations correspond to the same dust event. Due to the aforementioned inhomogeneity, a lidar ratio of 45sr (at 355nm) and 40sr (at 532nm), were considered to better fit the dust dominated scene during the Falcon overpass. These values are typical for the dust events above Finokalia station during the one-year operations of the system between 2017 and 2018.

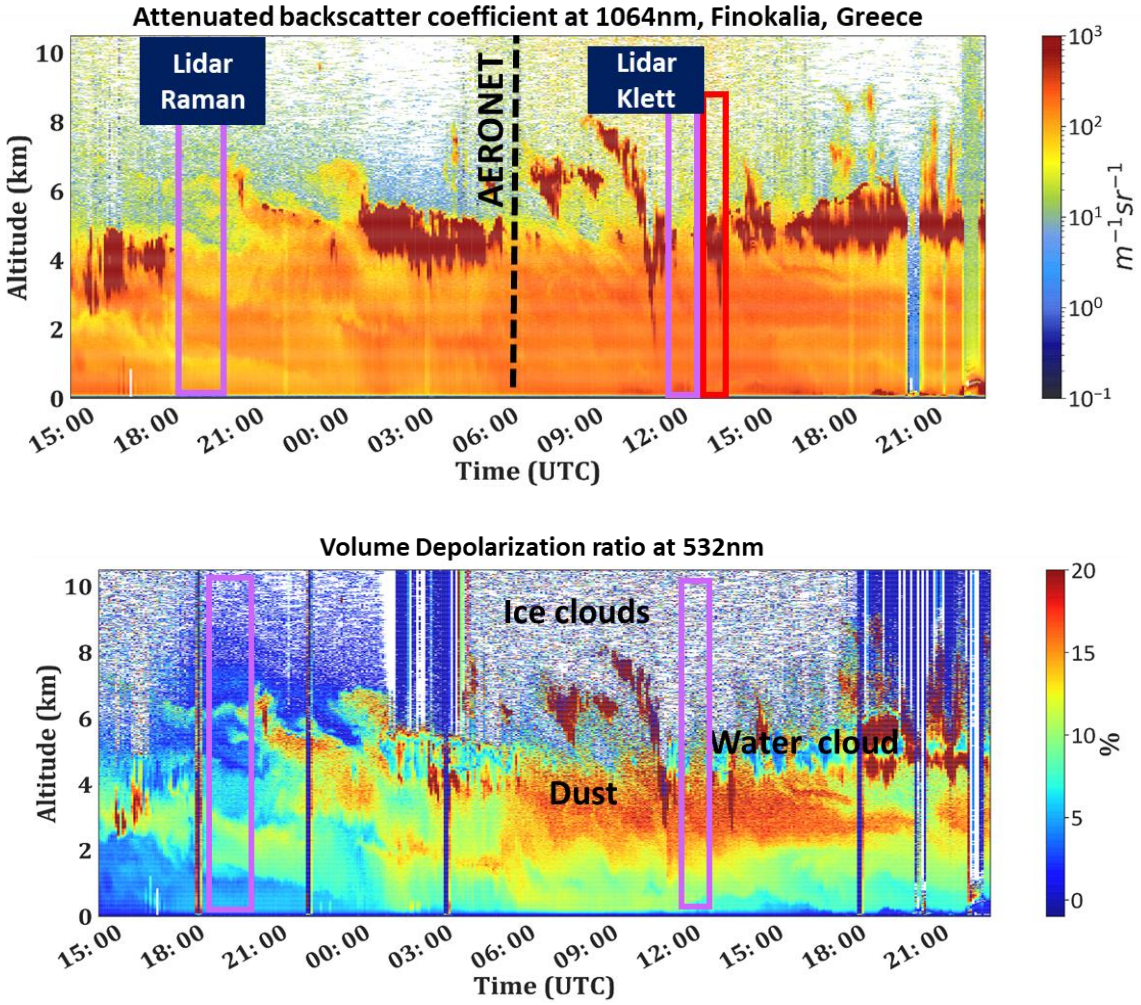

Figure 14 19 to 20 April 2017 (Crete): Time-height display of the 1064nm total attenuated backscatter coefficient (up) and the 532nm volume linear depolarization ratio (down). Night-time Raman measurements on 19 April 2017, 18:00 – 19:20 UTC were used to derive the lidar ratio values needed for the daytime inversions (20 April 2017, 11:25 - 12:00 UTC). Red box: the time period that Falcon overpass Crete.

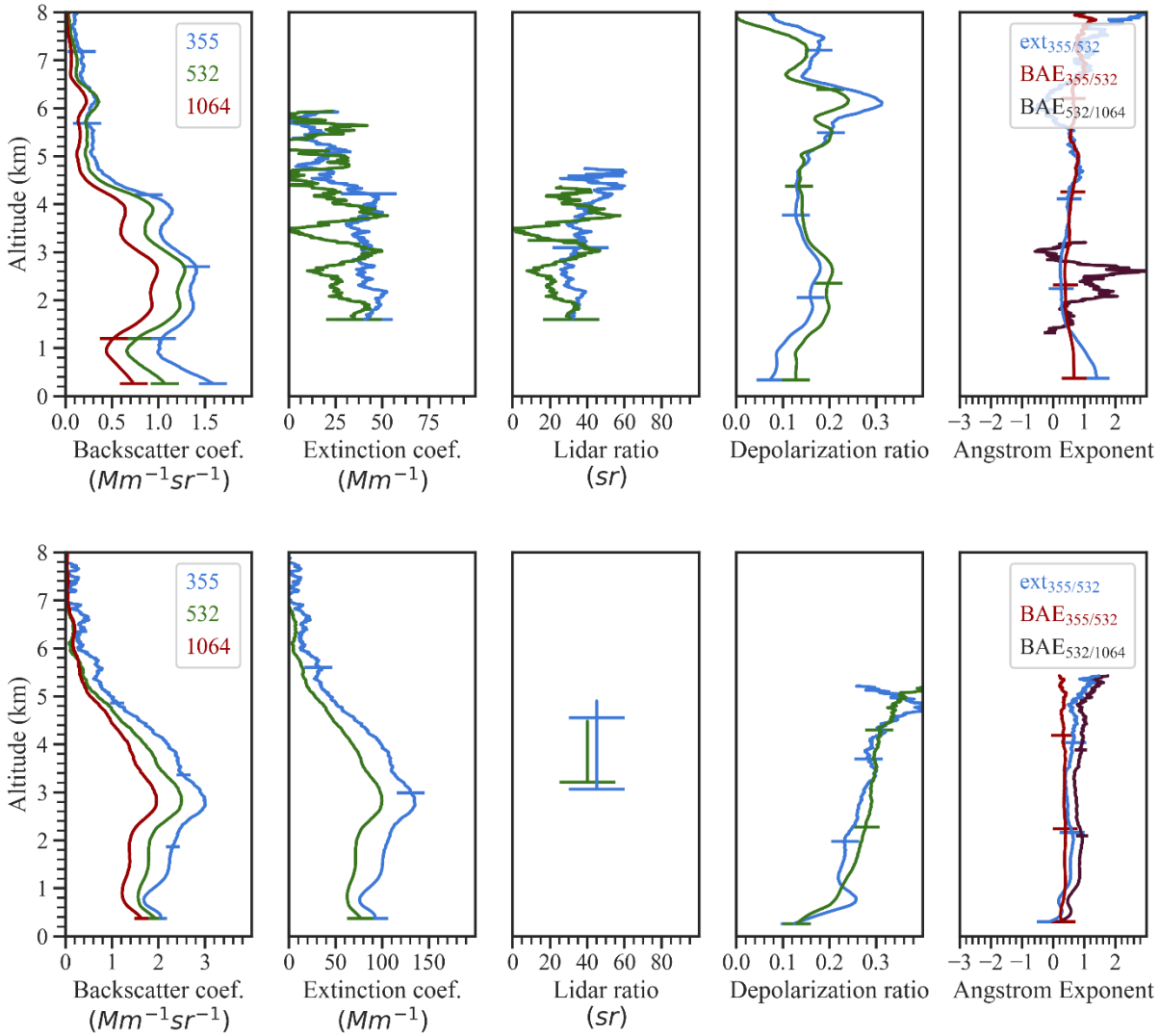

Figure 15 Optical properties measured with the lidar on 19 April 2017, 18:00 – 19:20 UTC (up) and 20 April 2017, 11:25 – 12:00 UTC (down). The upper panel displays the nighttime retrievals of the backscatter and extinction coefficient, the lidar ratio, particle linear depolarization ratio and the angstrom exponent. Lower panel displays the closest to the Falcon overflight, day-time retrievals of the backscatter and extinction coefficient, the LR assumption (dust typical values are considered instead of the preceding night-time lidar ratios), the particle linear depolarization ratio and the Angstrom exponent. Vertical smoothing window used for all optical properties is 533 and 383m for night-time and day-time retrievals respectively. The samples collected with Falcon on that case was at 2.957 km, 2.945km and 2.012km ase. All layer-mean intensive optical properties between 1.5 to 4.5km are summarized in Table 2.

Table 2. Layer-mean intensive optical properties and their uncertainties at 355 and 532 nm in blue and green on 20 April 2017. The aerosol sources are provided in the Raman cases by the modeled sources (Fig. 16) and in the Klett cases by the Falcon typing (Fig. 18).

Date, Time	**Height (Aerosol sources)**	**Meathod**	**Dep. Ratio (%)**	**Lidar ratio (sr)**
19 April, 18:00 – 19:20 UTC	1.5 – 4.7 km ase (*dust particles)*	Klett	28±6% 29±5%	45±18 40±16
20 April, 11:25 – 12:00 UTC	1.5 – 4.6 km ase* (*dust particles*)	Raman	15±3% 17±3%	36±6 27±5

*For the Raman Lidar ratio mean the height between 1.5 – 4.35 km is used.

Based on the meteorological analysis, a well-defined trough in the upper atmosphere located over the Central Mediterranean, associated with low pressures in the surface in North Sahara, led to southern flow and the transport of dusty air masses above Greece and Crete (Fig. 16a, b).

The FLEXPART-WRF source-receptor sensitivity study at the station reviled that the air masses arriving at 2.5 km above the station followed north-northwestern directions carrying marine particles mostly from the Aegean Sea, dust particles from the Sahara Desert along with possible contribution of pollution and continental particles from the Balkans (Fig. 16c).

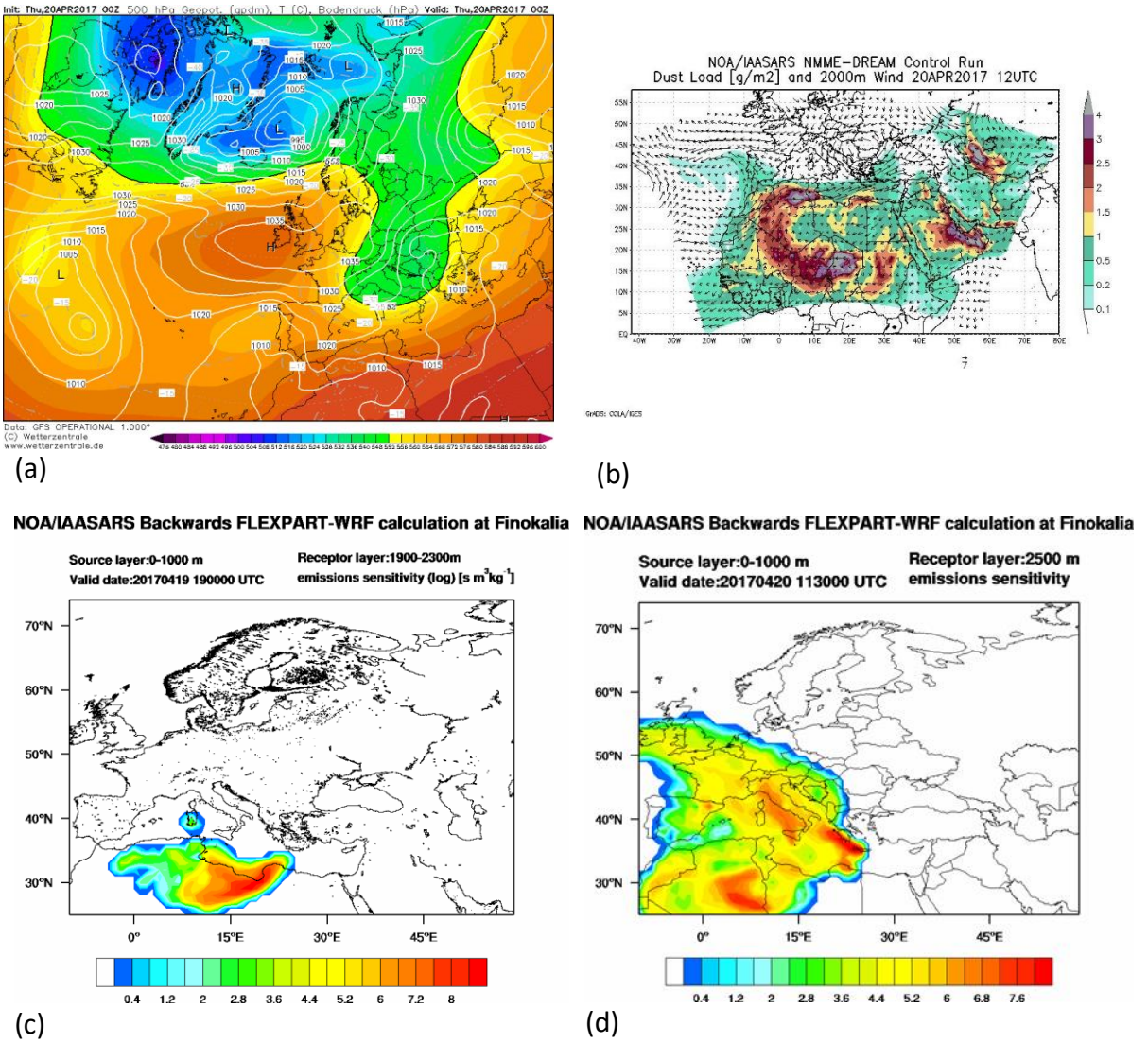

Figure 16 (a) Geopotential Height in 500hPa, along with isobars and surface isotherms on 20 April 00:00UTC (source: https://www.wetterzentrale.de/), (b) NMME-Dream Dust-load and wind direction at 2km height on 20 April 12:00 UTC, (c) Five-day backward FLEXPART-WRF calculation of emission sensitivity for the particles arriving at Finokalia on19 April 2017 19:00 UTC, at heights 1.9 to 2.3 km a.g.l., from source heights between 0 – 1 km a.g.l. (c) and on 20 April 2017 11:30 UTC, at heights 2.5 km a.g.l., from source heights between 0 – 1 km a.g.l.

The dominance of coarse-mode particles (both dust and marine aerosols) in the atmospheric column is also evident from the sun-photometer size distribution (Fig. 17), 8 hours before the Falcon overflight. No other AERONET inversions are available on this day due to extensive cloud cover.

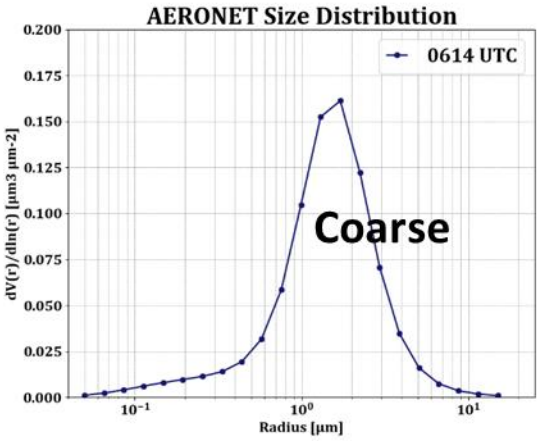

Figure 17 Volume size distribution derived from AERONET observations at Finokalia, on 20 April 2017 at 06:14 UTC. A dominant coarse mode is observed.

In the samples collected with the Falcon at 3.15km asl (2.9 km ase) mainly dust particles was found. With a small contribution of organic and sulfate component. In the sample from 2.2km asl, again dust is the dominant particle, observed (Fig. 18).

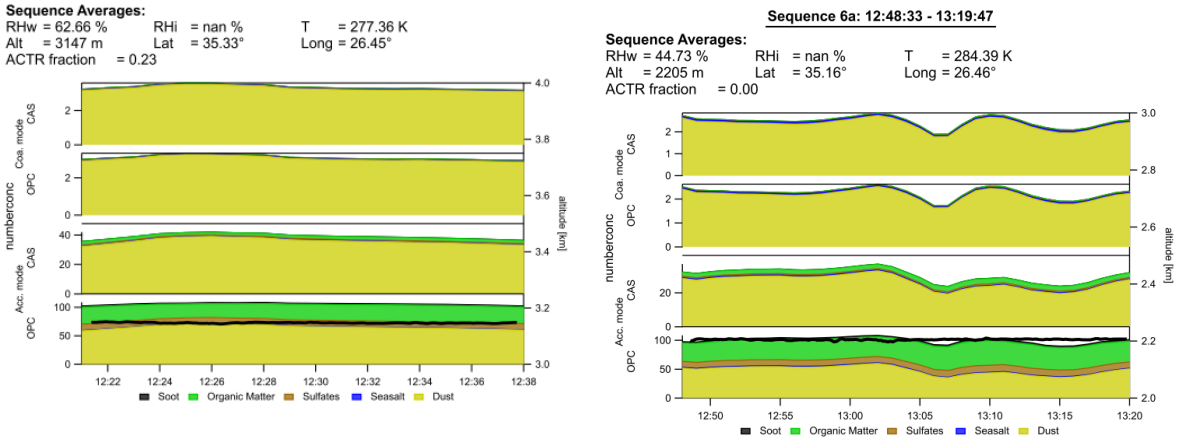

Figure 18 Chemical composition derived from in-situ samples on board Falcon at 3.15km.

Case 7 Saharan Dust – 20 April 2017 – Cyprus

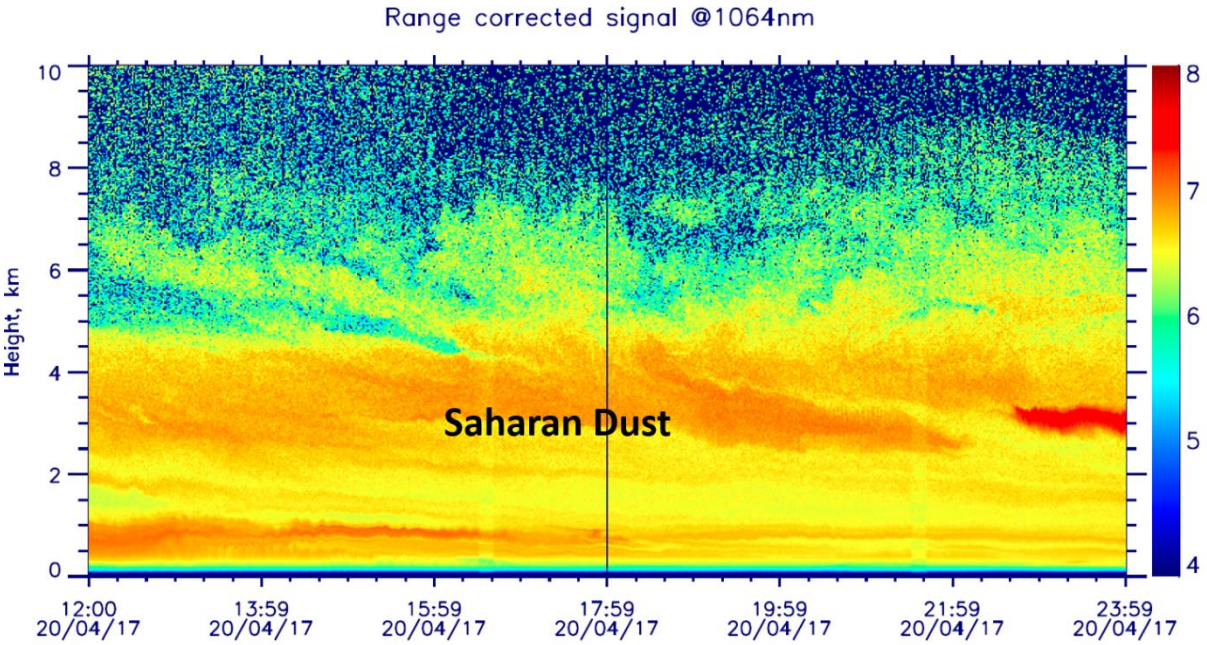

Figure 19 20 April 2017 (Cyprus)**:** Time-height display of the 1064 nm range corrected signal. Saharan dust layers were observed up to 9 km height. For the comparison the centre of the dust (3 - 5 km height) was used. Falcon measurements at 17:40 – 18:30 UTC were used.

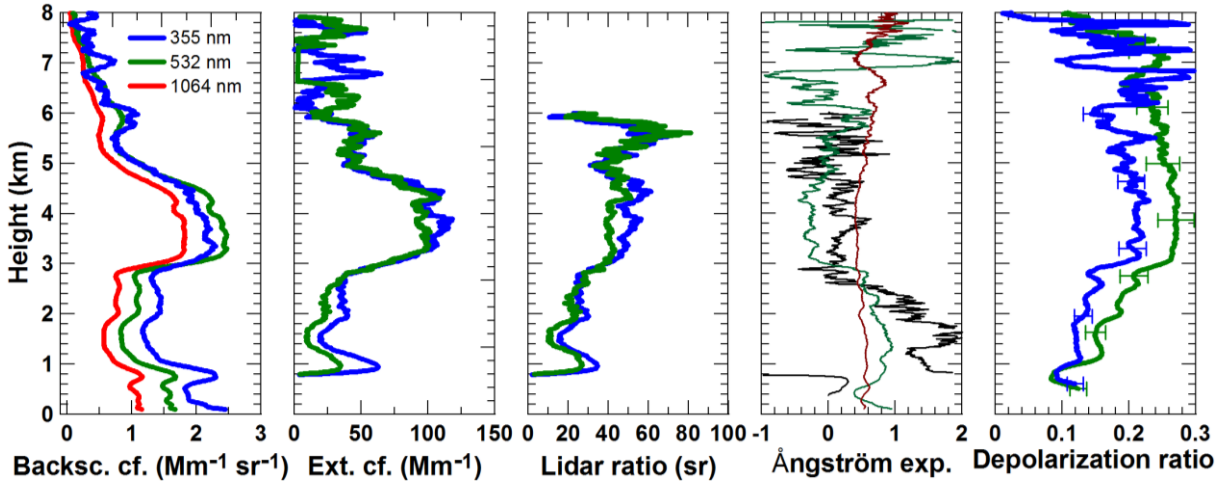

Figure 20 Optical properties measured with lidar on 20 April 2017, 17:00 - 19:00 UTC. The main dust layer between 3 and 5 km was used for comparison with Falcon.

Case 8 Saharan Dust – 21 April 2017 – Cyprus

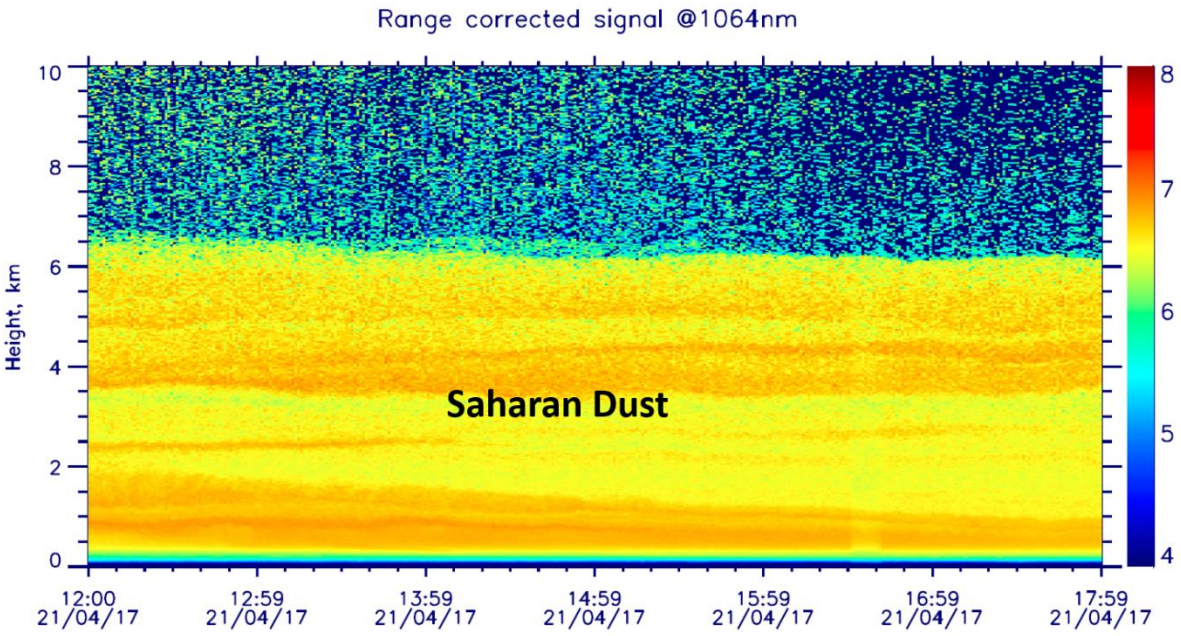

Figure 21 21 April 2017 (Cyprus)**:** Time-height display of the 1064 nm range corrected signal. Saharan dust layers were observed 6.5 km height. For the comparison the stronger dust layer (4 - 6 km height) was used. Falcon measurements at 11:50 – 16:00 UTC were used.

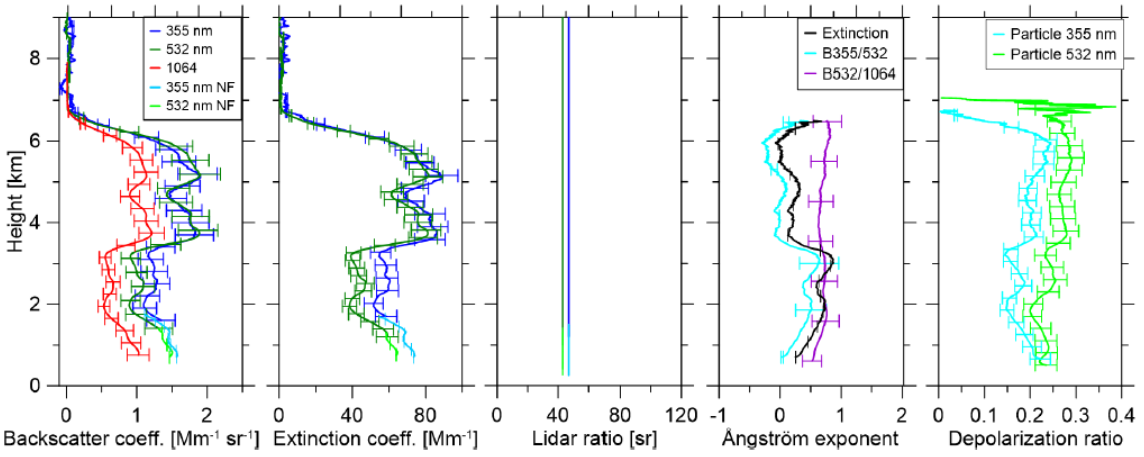

Figure 22 Optical properties measured with lidar on 21 April 2017, 11:50 - 16:00 UTC. The main dust layer between 4 and 6 km was used for comparison with Falcon. The lidar ratios of the dust layer were determined using night-time Raman observations (17:00 - 20:00 UTC).

Case 9 Pollution from the North – 25 April 2017 – Cyprus

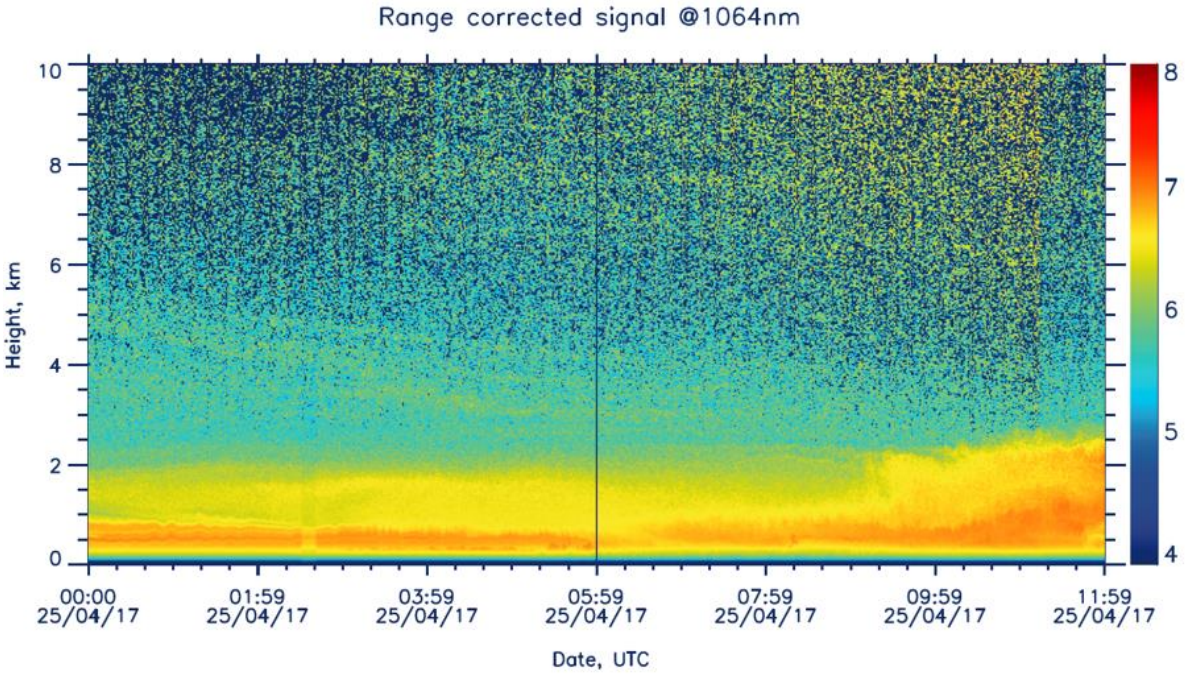

Figure 23 25 April 2017 (Cyprus)**:** Time-height display of the 1064 nm range corrected signal. Pollution originating from the north (Turkey) were observed up to 2.0 km height. For the comparison the pollution layer at 1 – 2 km height was used. Falcon measurements at around 08:00 UTC were used.

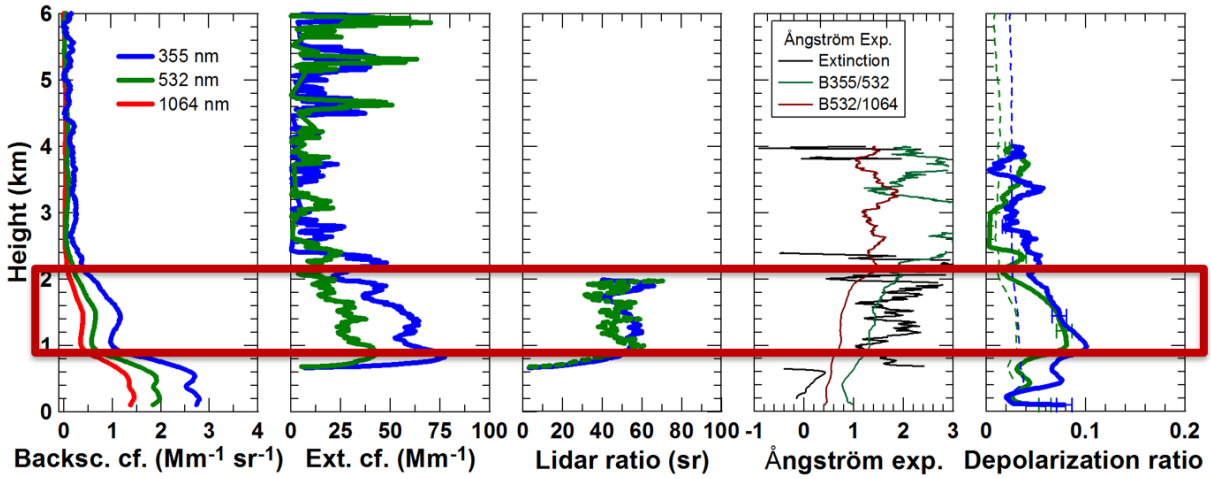

Figure 24 Optical properties measured with lidar on 25 April 2017, 00:00 – 03:00 UTC. The pollution layer at 1.0 – 2.0 km height was used. Night-time Raman lidar observations are shown, from which the lidar ratio was derived to be used for the simultaneous observations to Falcon aircraft.

Case 10 Middle Eastern Dust – 27 April 2017 – Cyprus

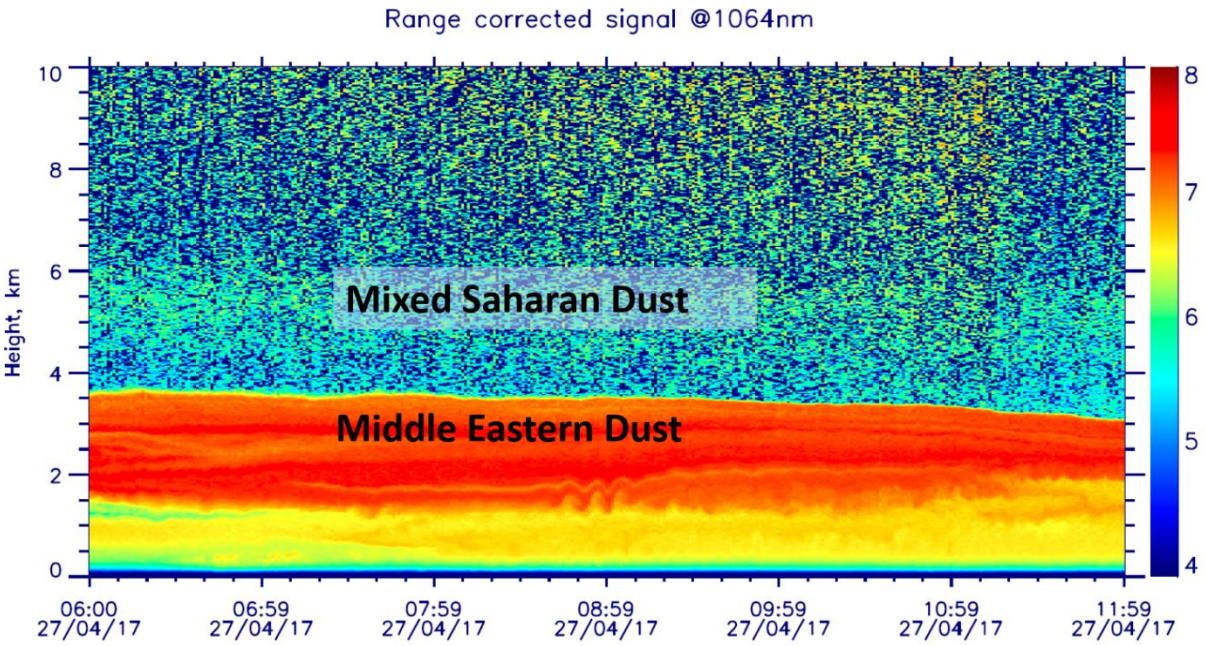

Figure 25 27 April 2017 (Cyprus)**:** Time-height display of the 1064 nm range corrected signal. An optically thick dust layer originating from the Middle East extended from 1.5 to 3.5 km height. Falcon measurements at around 07:15 – 07:50 UTC were used.

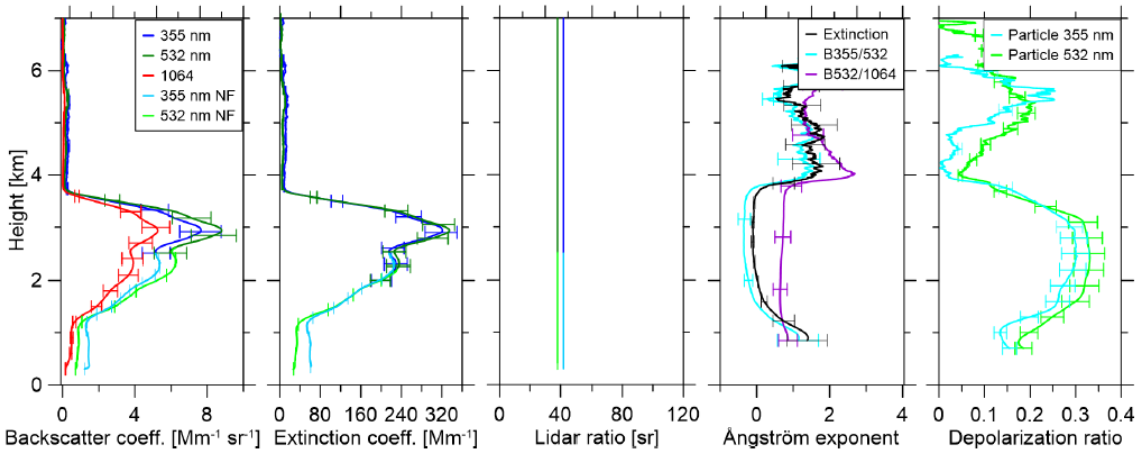

Figure 26 Optical properties measured with lidar on 27 April 2017, 07:15 – 10:15 UTC. The strong dust layer reached extinction values of up to 300 Mm^{-1}, height from 1.5 to 3.8 km were used for comparison. The lidar ratios of the dust layer were determined using night-time Raman observations.

Case 11 – 29 April 2017 – Crete

The temporal development of the attenuated backscatter coefficient and the volume linear depolarization ratio on 29 April 2017 is shown in Fig. 27. A well stable aerosol layer bellow 2 km is observed all day. Elevated aerosol layers were observed above the station starting in the up to 8 km. In the beginning of the day, the att. Bp. Coeff. and volume depolarization ratio of these layers have low values which are increased within the day. Clouds are observed above 8km from 06:00 onward, while cloud bottom reaches to about 4km by the end of the day. The time of the Falcon sampling was between 8:31 – 10:15 UTC, and collected five samples between 2.2 km to 6.6 km (Black boxes in the plot). Raman measurements on 00:00 – 02:00 UTC were used to derive the particle lidar ratio needed for the daytime retrievals, on 12:55 - 14:55 UTC, close in time to the Falcon overflight. Both the overflight and the daytime lidar profiles are conducted in the presence of the thin elevated layers. From the attenuated backscatter plot we see slight difference in the intensity and vertical extend of the layers. From the volume depolarization plot we see that the aerosol depolarizing component is more dominant during the time of the lidar Klett retrieval in comparison to the time of the overflight or the night-time retrieval. During nighttime, different lidar ratio values are observed for the lower layer (~between 0.5 and 1.5 km) and the upper layer (above 3.5km). Noisy signals at the altitude of the upper layer, limit our confidence on the retrieved lidar ratio values at 532nm. For the daytime retrievals, we used the literature values of 40±16 Sr at 532nm.

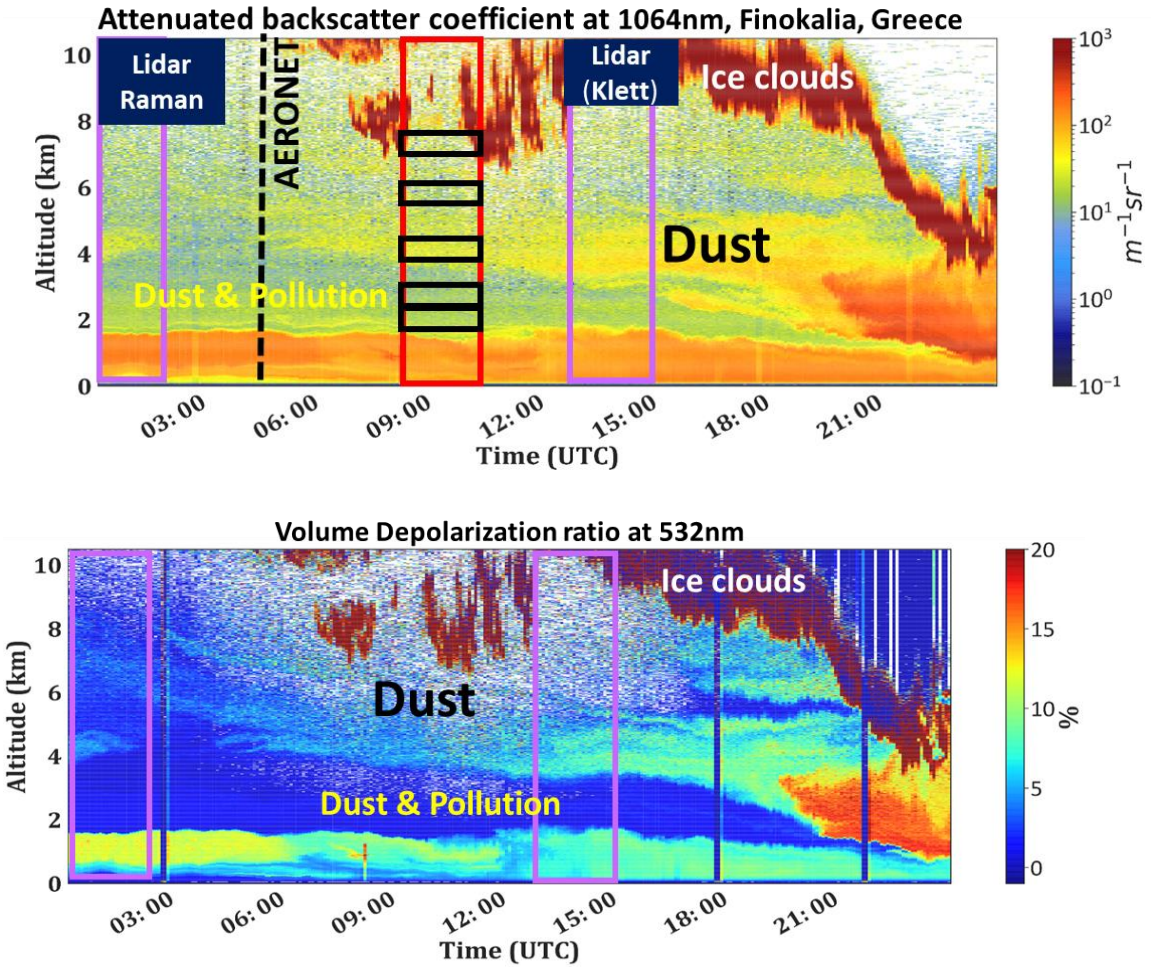

Figure 27 29 April 2017 (Crete): Time-height display of the 1064nm total attenuated backscatter coefficient (up) and the 532nm volume linear depolarization ratio (down). Night-time Raman measurements on 00:00 – 02:00 UTC were used to derive the lidar ratio values needed for the daytime inversions close to the Falcon overflight (29 April 2017, 12:55 – 14:55 UTC).

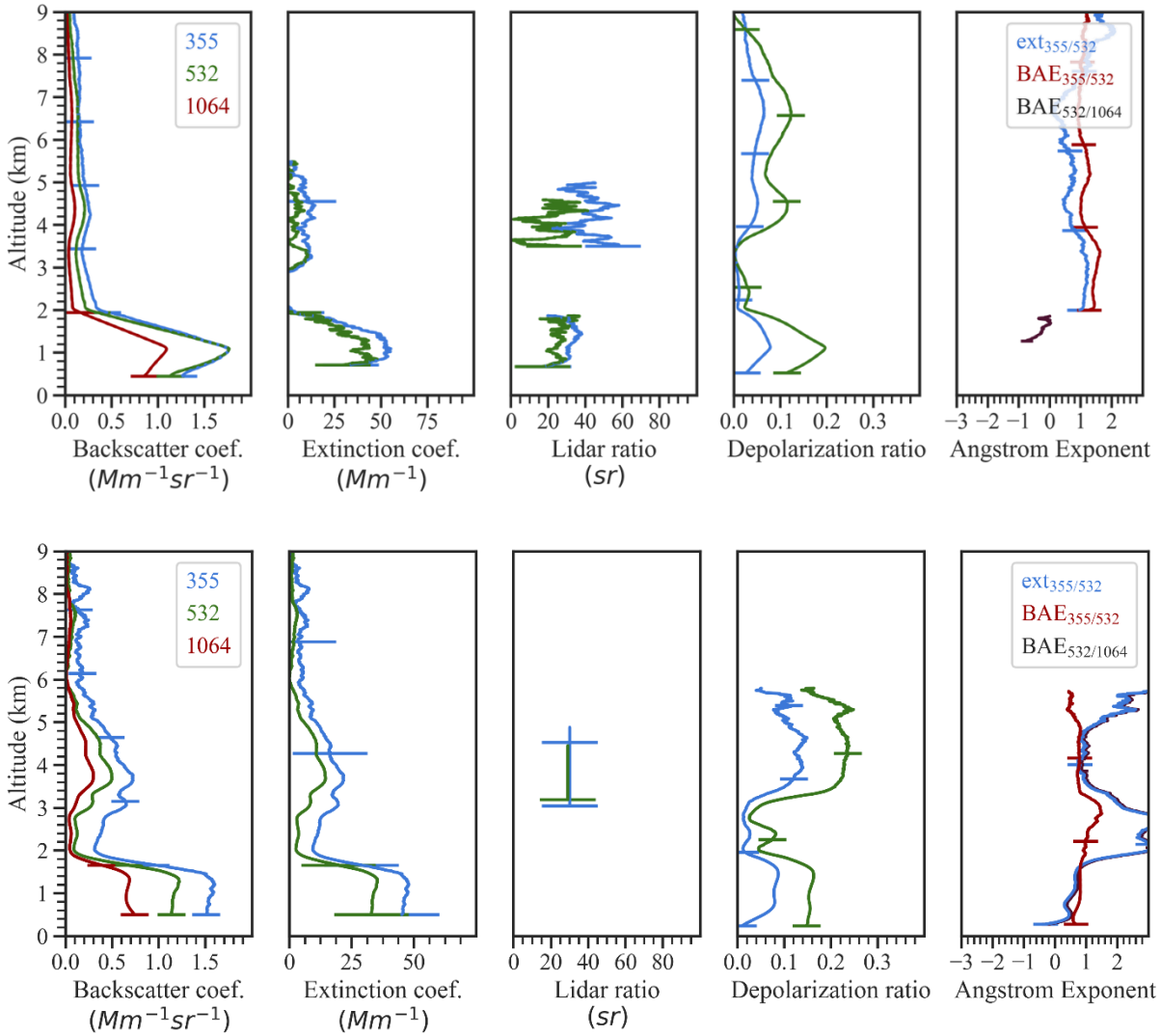

Figure 28 Optical properties measured with lidar on 29 April 2017, 00:00 – 02:00 UTC (up) and 12:55 – 14:55 UTC (down). The upper panel displays the night-time retrievals of the backscatter and extinction coefficient, the lidar ratio, particle linear depolarization ratio and the angstrom exponent. Lower panel displays the closest available to Falcon overflight, day-time retrievals of the backscatter and extinction coefficient, the lidar ratio assumption, the particle linear depolarization ratio and the Angstrom exponent. Vertical smoothing window used for all optical properties is 908 m and 338 m for night-time and day-time retrievals respectively.

Between the two retrievals, only the lowermost part of the scene can be considered homogenous, while temporal stability does not hold for the Falcon flight altitudes. Nevertheless, the derived lidar ratio values for the layer found between 4 and 5km are close to those expected for dust, while downward dust mixing is revealed by both increased lidar ratio and depolarization ratio values inside the marine boundary layer. Layer-mean intensive optical properties at 0.5 – 1.5, 3 – 6 and 4 – 5 km are summarized in Table 3.

Table 3. Layer-mean intensive optical properties and their uncertainties at 355 and 532 nm in blue and green at 0.5 – 1.5, 3 – 6 and 4 – 5km on 20 April 2017. The aerosol sources for the altitudes < 2 km and for the Raman cases are provided by the modeled sources (Fig. 29) and in the Klett cases > 2 km by the Falcon typing (Fig. 31).

Date, Time	Height (Aerosol sources)	Meathod	Dep. Ratio (%)	Lidar ratio (sr)
29 April, 00:00 – 02:00 UTC	0.8 – 1.8 km ase (marine + pollution + continental)	Raman	7±5%* 17±5%*	33±13 26±16
	2-3 km ase (dust + pollution)	Raman	1.0±0.3% 2.8±0.8%	
	4 – 5 km ase (dust)	Raman	5±3% 9±3%	
29 April, 12:55 – 14:55 UTC	0.5 – 1.5 km ase (marine + pollution + continental)	Klett	8.3±2% 14±5%	30±12 29±12
	2-3 km ase (dust + sulfate + organic)	Klett	1.7±0.7% 5.2±0.7%	
	3.5 – 5.6 km ase (dust)	Klett	15±3% 20±2%	45±14 40±16

* For the Depol. Ratio mean the height between 1.8 – 1.65 km is used.

Based on the meteorological analysis, a deep trough crossed South Europe and Mediterranean starting from 27 April 2017 reaching Italy and Greece on 29 April. Dust was transported by the associated strong, northern winds towards Italy and Greece (Fig. 29a, b). Based on FLEXPART-WRF source-receptor sensitivity study at the station, at altitudes between 1.5 and 5 km, a mixture of marine particles from the Aegean along with possible contribution of pollution and continental particles from Turkey is present at the lowermost part of the profile (Fig. 29c), whereas at 5 km the dominant aerosol types were dust transported from Morocco and North Algeria and pollution/continental transport from Turkey (Fig. 29d).

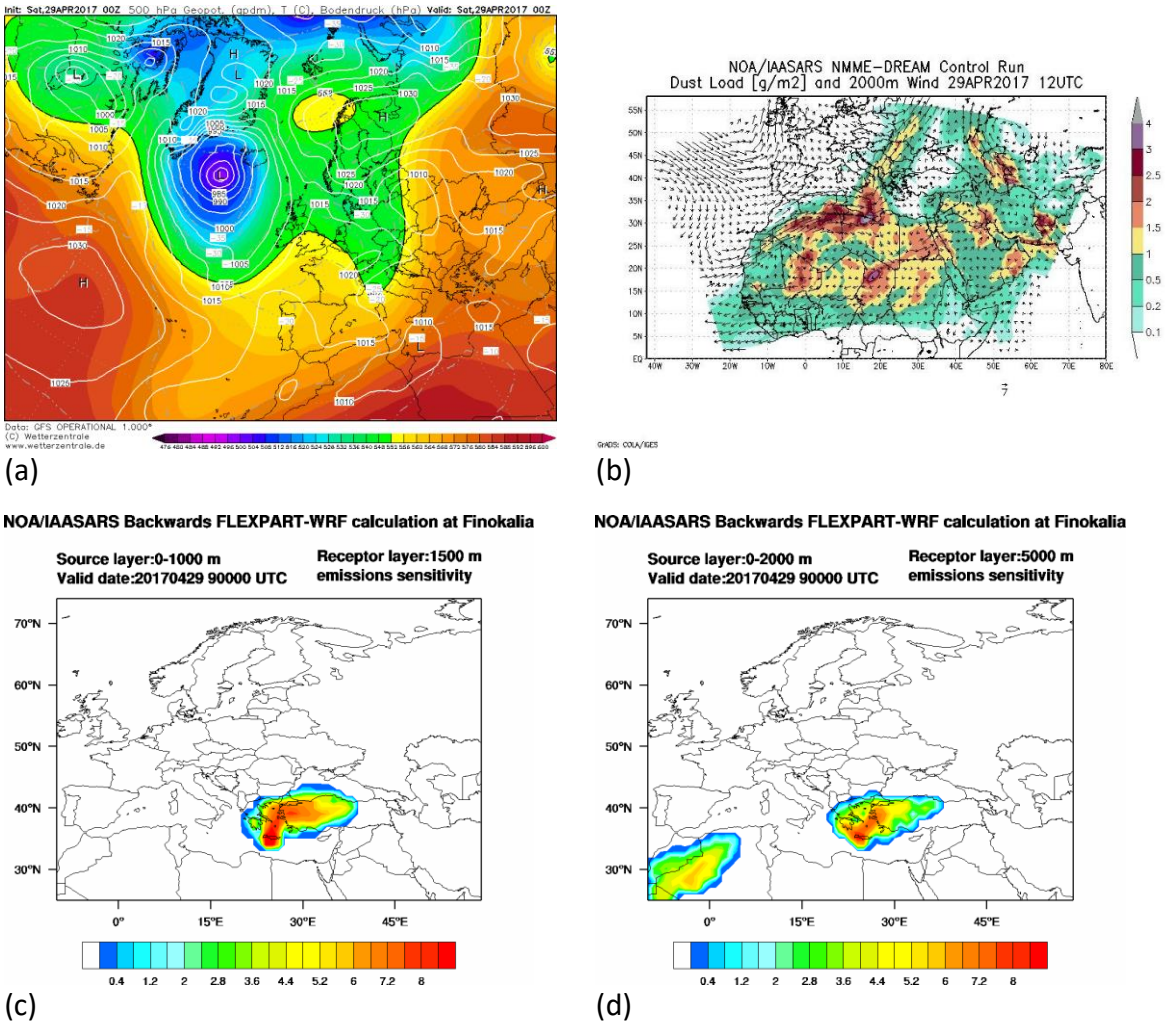

Figure 29 (a) Geopotential Height in 500hPa, along with isobars and surface isotherms on 29 April 00:00UTC (source: https://www.wetterzentrale.de/), (b) NMME-Dream Dust-load and wind direction at 2 km height on 29 April 12:00 UTC, (c) Five-day backward FLEXPART-WRF calculation of emission sensitivity for the particles arriving at Finokalia on 29 April 2017 09:00 UTC, at heights 1.5 km a.g.l., from source heights between 0 – 1 km a.g.l. ans (d) and at heights 5 km a.g.l., from source heights between 0 – 2 km a.g.l.

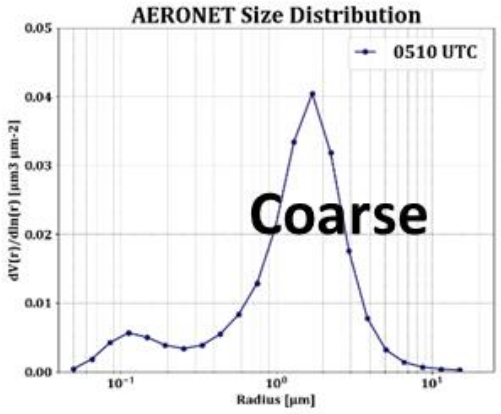

Figure 30 Volume size distribution derived from AERONET observations at Finokalia, on 29 April 2017 at 05:10 UTC. A dominant coarse mode is observed.

The dominance of coarse-mode particles (both dust and marine aerosols) in the atmospheric column is also evident from the sun-photometer size distribution (Fig. 30), 4 hours before the

Falcon overflight. No other AERONET inversions are available on this day due to extensive cloud cover.

For the comparison with the lidar data, Falcon measurements at 2.2, 2.8, 4, 6 and 6.6 km were used. Chemical analysis of the in-situ data shows mainly dust contribution at all flight altitudes, along with sulfates and organic matter mainly at the lowermost part of the atmospheric column (Fig. 31).

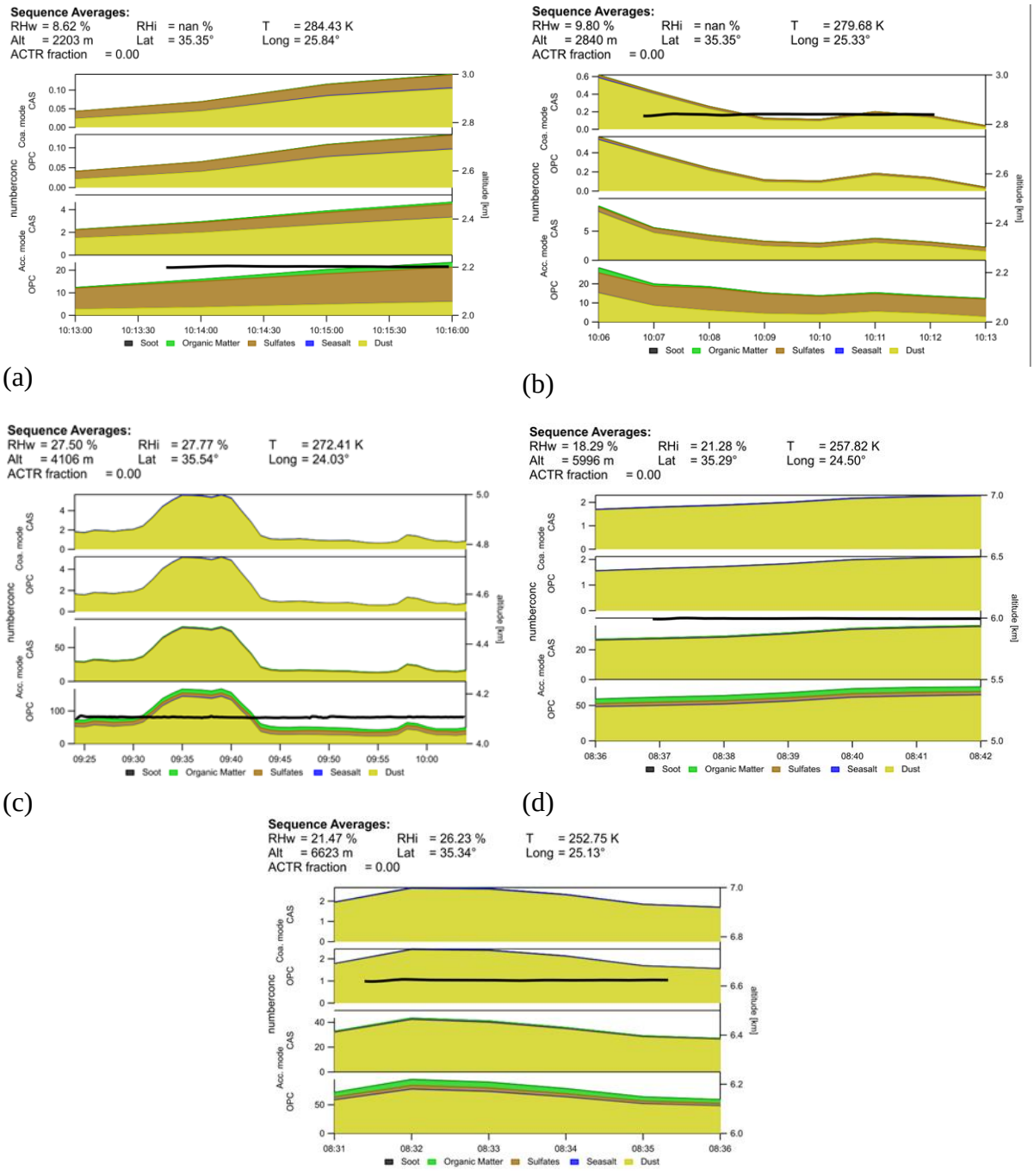

(a) (b)

(c) (d)

(e)

Figure 31 Chemical composition derived from in-situ samples on board Falcon at 2.2, 2.8, 4, 6 and 6.6 km asl.

4. DATA ANALYSIS

4.1 From optical properties to size distribution

Vertically resolved aerosol classification is of great importance for improved measurement retrievals, quantification of both the anthropogenic and the natural radiative effect, radiative closure and aerosol-cloud interaction studies, as well as data assimilation and satellite validation purposes.

The applied novel retrieval scheme uses the optimal estimation method (OEM) to a combination of lidar-derived intensive aerosol properties, to determine the statistically most-likely contribution of aerosol component to the observed aerosol mixture. The four aerosol components considered to contribute to an aerosol mixture are two fine modes (absorbing (FSA) and non-absorbing (FNA)) and two coarse modes (spherical (CS) and non-spherical (CNS)) as described in Wandinger et al., 2016. These four components and their optical properties have been selected from lidar-based experimental bases at 355 and 532 nm. Using an initial guess, the lidar ratio, particle linear depolarization ratio and extinction-related Ångström exponent are calculated (forward modelling for the wavelengths 355 nm, or 532 nm or both simultaneously) and then compared with the lidar measurements. If they match within an acceptable range the process stops, otherwise the iterative process continues, adjusting the solution at each step until convergence is met. The final product is the contribution of the four aerosol components to an aerosol mixture in terms of relative volume. Once this product meets certain quality assurance flags (Pearson's chi-squared test) it can be used to provide additional products: (a) aerosol component separated backscatter and extinction profiles, (b) aerosol optical depth per aerosol component, (c) volume concentration per component, (d) number concentration per component, (e) effective radius of the observed mixture and (f) refractive index of the mixture.

A-CARE provided the unique opportunity to compare the retrieved aerosol mixture in terms of number and volume size distributions, as well as the effective radius to coincident airborne in situ observations.
The layer-mean optical properties of the presented 11 case studies are summarized in Table and visualized in Figure 32. They span well over the entire space, except of pure marine and pure smoke conditions. The aim of using the Eastern Mediterranean was to characterize a lot of mixtures to test the classification algorithm.
In a next step, the optimal estimation algorithm is applied to retrieve the optimal mixing of the four aerosol components (Table). The volume concentration of each component is calculated scaling the prescribed size distribution with the actual measured extinction coefficient. The results are summarized in Table .

Table 4 Layer mean optical properties and their uncertainties at 355 and 532 nm in blue and green from lidar observations for the 11 selected cases.

Case	Date	Source	Height (km)	Dep. ratio (%)	Lidar ratio (sr)
1	6 April	Sahara	2– 4	15.6 ± 0.6 19.3 ± 0.6	38 ± 6 33 ± 6
2	6 April	Arabia	< 1	17.2 ± 0.6 19.8 ± 0.9	42 ± 7 38 ± 6
3	11 April	Local	1.0 – 1.5	7.3 ± 0.8 2.9 ± 0.9	75 ± 14 74 ± 28
4	14 April	Local	1.0 – 2.5	3.1 ± 0.7 2.2 ± 0.2	55 ± 10 39 ± 10
5	14 April	Marine + Pollution	0.9 – 1.3	5.1 ± 0.3 2.6 ± 0.3	36 ± 6 33 ± 8
6	20 April	Pollution + Sahara	2.5 – 3.5	16.2 ± 1.3 18.4 ± 2.0	33 ± 4 22 ± 10
7	20 April	Sahara	3 – 5 (1 – 9)	20.6 ± 1.2 26.4 ± 0.8	49 ± 8 44 ± 7
8	21 April	Sahara	4 – 6	21.3 ± 2.0 27.7 ± 1.0	53 ± 8 46 ± 9
9	25 April	Pollution from the North	1 – 2 km	7.4 ± 1.0 6.7 ± 1.1	38 ± 6 34 ± 5
10	27 April	Arabia/ Middle East	1.5 – 3.8	28.5 ± 1.5 32.3 ± 0.9	38 ± 6 34 ± 5
11	29 April		3.8 – 5.5	4.3 ± 0.6 8.8 ± 1.9	35 ± 13 13 ± 15

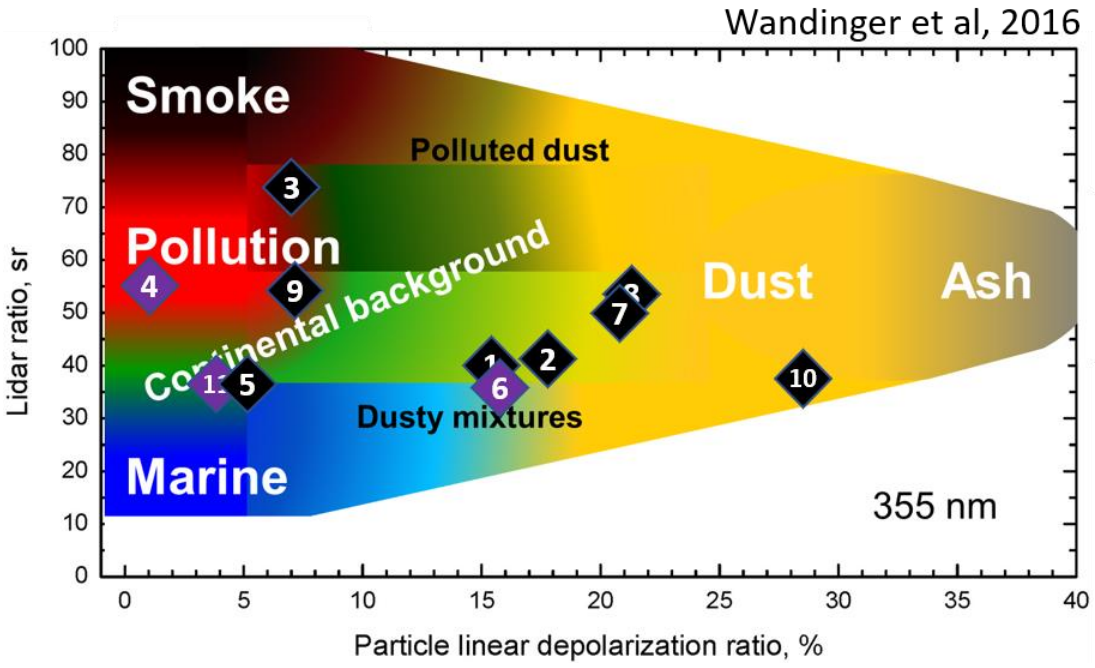

Figure 32 Visualisation of the 11 cases in the lidar ratio – particle linear depolarization ratio space used for aerosol type classification in HETEAC (Wandinger et al., 2016). The 11 selected cases span quite well over the entire space, except of pure marine and pure smoke conditions. The aim of using the Eastern Mediterranean was to characterize a lot of mixtures to test the classification algorithm.

Table 4 Contribution of the four basic aerosol components to the aerosol mixture, if the optimal estimation method found a statically significant solution. The four components are FSA – fine mode strongly absorbing ("Smoke"), CS – coarse mode spherical ("Marine"), FNA – fine mode non-absorbing ("Pollution"), CNS – coarse mode non-spherical ("Dust"). Due to the uncertainties which are provided of the optimal estimation algorithm, the sum is not always exactly 100%. For case 6 no statistically significant solution was found.

Case	FSA (%)	CS (%)	FNA (%)	CNS (%)
1*	0.0 ± 4.6	21.1 ± 8.2	0.0 ± 6.8	77.5 ± 21.6
2*	0.0 ± 4.1	18.6 ± 7.3	0.0 ± 6.1	81.0 ± 21.8
3	66.5 ± 21.4	18.7 ± 15.1	12.4 ± 20.5	2.4 ± 5.5
4	3.6 ± 19.1	6.1 ± 21.8	87.2 ± 22.3	3.2 ± 18.7
5	6.8 ± 11.3	77.8 ± 22.1	5.4 ± 19.7	10.0 ± 14.4
6	--	--	--	--
7	0.0 ± 8.5	3.5 ± 18.3	10.1 ± 11.1	86.1 ± 22.2
8	1.8 ± 8.5	1.7 ± 18.3	8.9 ± 11.0	87.6 ± 22.2
9	2.9 ± 9.4	27.8 ± 17.4	28.0 ± 18.5	41.4 ± 16.6
10*	0.0 ± 10.9	8.0 ± 12.9	0.6 ± 15.7	91.3 ± 22.3
11	5.2 ± 10.9	77.1 ± 22.1	4.1 ± 19.6	13.6 ± 11.9

* not statistically significant within the 95% confidence interval

Table 6 Volume contribution of each of the four basic aerosol types and effective radius of the corresponding aerosol mixture**.** The four components are FSA – fine mode strongly absorbing ("Smoke"), CS – coarse mode spherical ("Marine"), FNA – fine mode non-absorbing ("Pollution"), CNS – coarse mode non-spherical ("Dust"). For case 6 no statistically significant solution was found.

Case	Volume FSA ($\mu m^3/cm^3$)	Volume CS ($\mu m^3/cm^3$)	Volume FNA ($\mu m^3/cm^3$)	Volume CNS ($\mu m^3/cm^3$)	Eff. Radius (μm)
1*	0.00	8.12	0.00	30.29	1.9371
2*	0.00	8.87	0.00	39.79	1.9371
3	96.03	2.29	15.68	0.38	0.1775
4	13.51	1.68	263.99	0.88	0.1542
5	56.98	52.57	36.56	7.09	0.7672
6	0.00	0.00	0.00	0.00	--
7	0.00	2.81	76.10	63.47	0.8531
8	19.90	1.65	80.44	75.41	0.8079
9	17.91	13.84	150.18	21.33	0.392
10*	0.00	13.14	17.81	157.20	1.7187
11	4.39	5.59	3.15	1.07	0.9037

* not statistically significant within the 95% confidence interval

4.2 Comparison of Size Distribution

A-CARE provided the unique opportunity to compare the retrieved aerosol mixture in terms of number and volume size distributions, as well as the effective radius to coincident airborne in situ observations.

Shown here are the volume size distributions derived from lidar measurements using the optimal estimation technique. The in situ measured number size distributions are transferred to volume size distributions under the assumption of spherical particles. The number size distributions are compared as well, but not shown in this report.

Additionally, the effective diameters are indicated by vertical dashed lines. The in situ effective diameter is derived using the size range 0.3 – 50 µm, the lidar derived effective diameter includes the smaller particles as well. Estimates of the uncertainty of the effective diameter will be provided for lidar and in situ in near future.

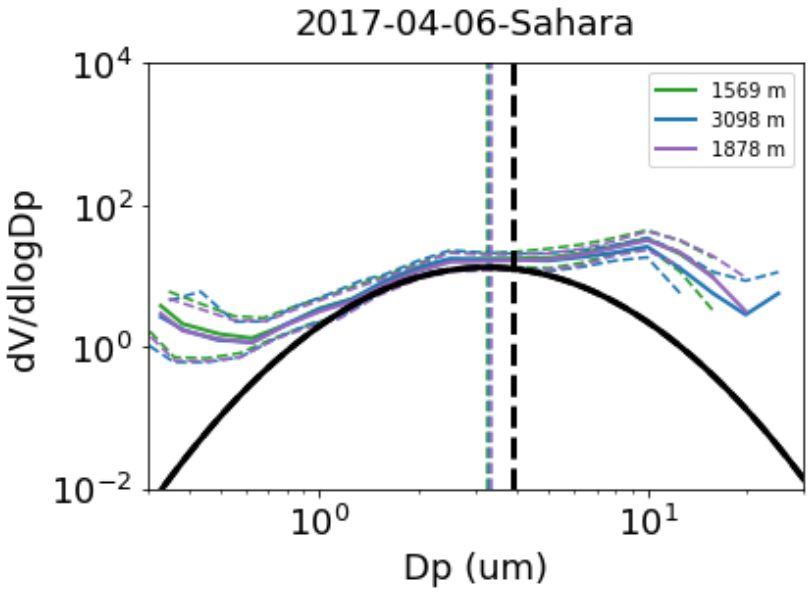

Figure 33 Case 1: Volume size distribution derived from lidar measurements (2 – 4 km height) using optimal estimation for aerosol type separation (black line) compared to size distributions measured on board of Falcon at various height levels (coloured lines). The dashed vertical lines indicate the effective diameter. Optimal estimation results were not statistically significant within the 95% confidence interval. Therefore, no uncertainty estimates are provided.

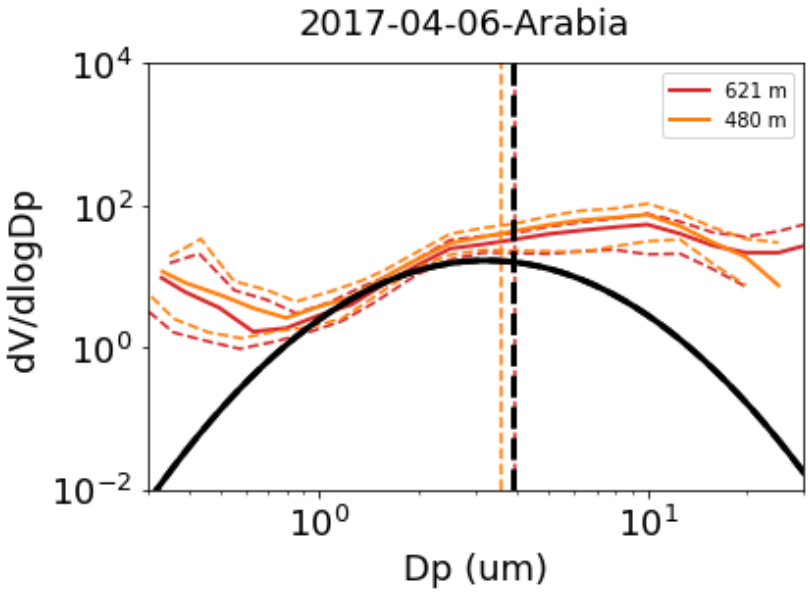

Figure 34 Case 2: Volume size distribution derived from lidar measurements (<1 km height) using optimal estimation for aerosol type separation (black line) compared to size distributions measured on board of Falcon at various height levels (coloured lines). The dashed vertical lines indicate the effective diameter. Optimal estimation results were not statistically significant within the 95% confidence interval. Therefore, no uncertainty estimates are provided.

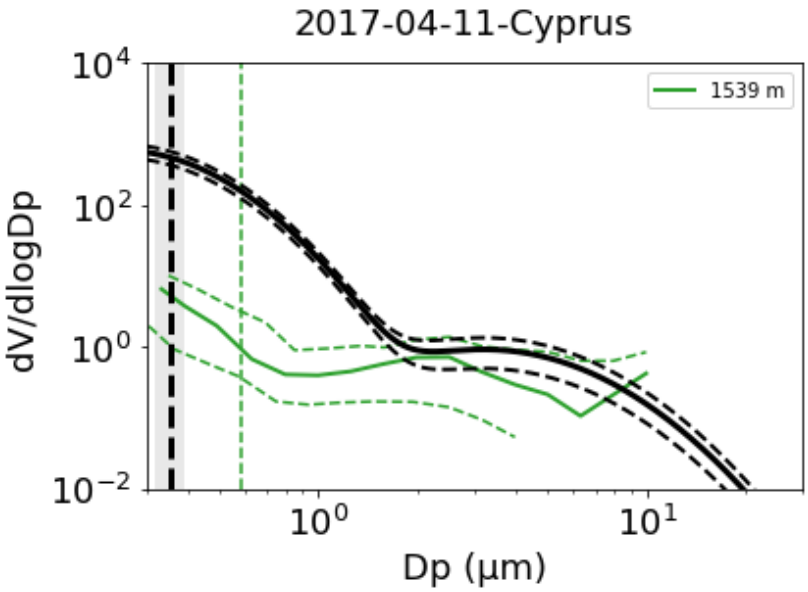

Figure 35 Case 3: Volume size distribution derived from lidar measurements (1.0 – 1.5 km height) using optimal estimation for aerosol type separation (black line, dashed lines indicate the uncertainty) compared to size distributions measured on board of Falcon at various height levels (coloured lines). The dashed vertical lines indicate the effective diameter, the shaded area the uncertainty of the effective diameter.

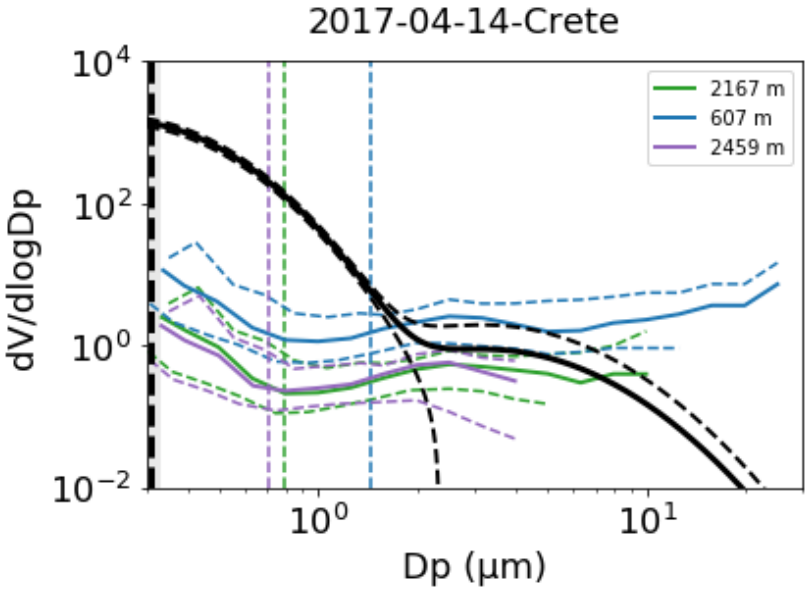

Figure 36 Case 4: Volume size distribution derived from lidar measurements (1.0 – 2.5 km height) using optimal estimation for aerosol type separation (black line, dashed lines indicate the uncertainty) compared to size distributions measured on board of Falcon at various height levels (coloured lines). The dashed vertical lines indicate the effective diameter, the shaded area the uncertainty of the effective diameter.

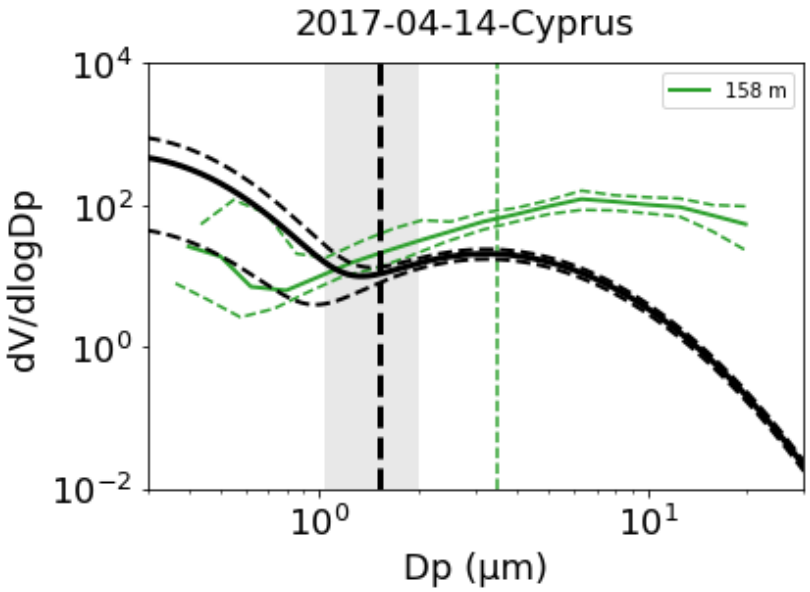

Figure 37 Case 5: Volume size distribution derived from lidar measurements (0.9 – 1.3 km height) using optimal estimation for aerosol type separation (black line, dashed lines indicate the uncertainty) compared to size distributions measured on board of Falcon at various height levels (coloured lines). The dashed vertical lines indicate the effective diameter, the shaded area the uncertainty of the effective diameter.

For Case 6, no statically significant solution was found. Therefore, it is not compared to the in-situ observations.

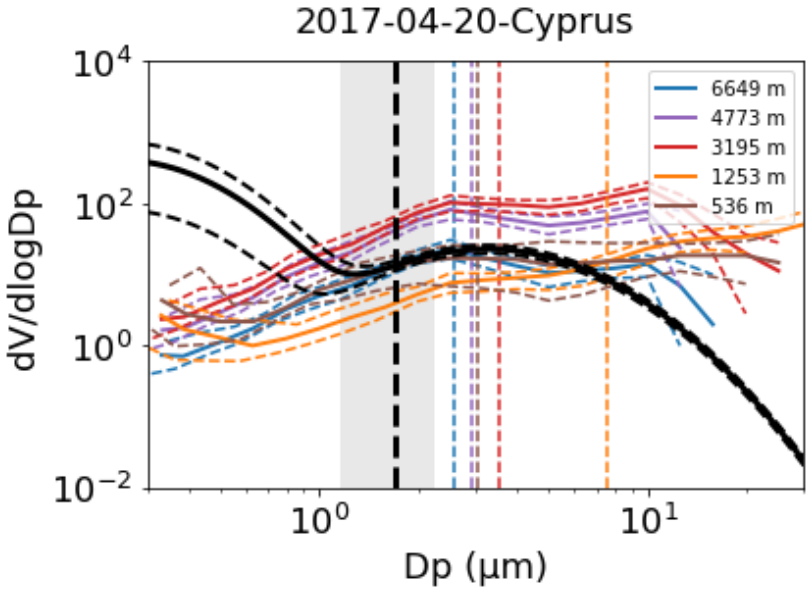

Figure 38 Case 7: Volume size distribution derived from lidar measurements (3 – 5 km height) using optimal estimation for aerosol type separation (black line, dashed lines indicate the uncertainty) compared to size distributions measured on board of Falcon at various height levels (coloured lines). The dashed vertical lines indicate the effective diameter, the shaded area the uncertainty of the effective diameter.

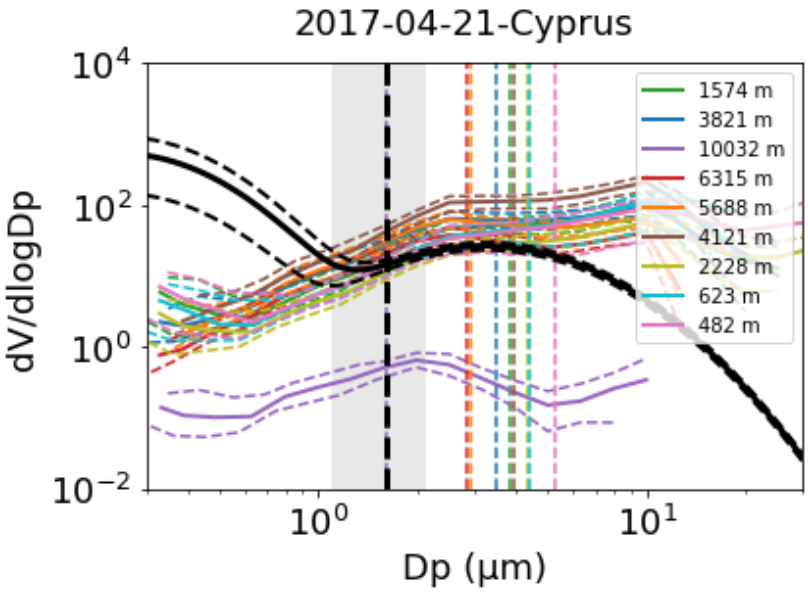

Figure 39 Case 8: Volume size distribution derived from lidar measurements (4 – 6 km height) using optimal estimation for aerosol type separation (black line, dashed lines indicate the uncertainty) compared to size distributions measured on board of Falcon at various height levels (coloured lines). The dashed vertical lines indicate the effective diameter, the shaded area the uncertainty of the effective diameter.

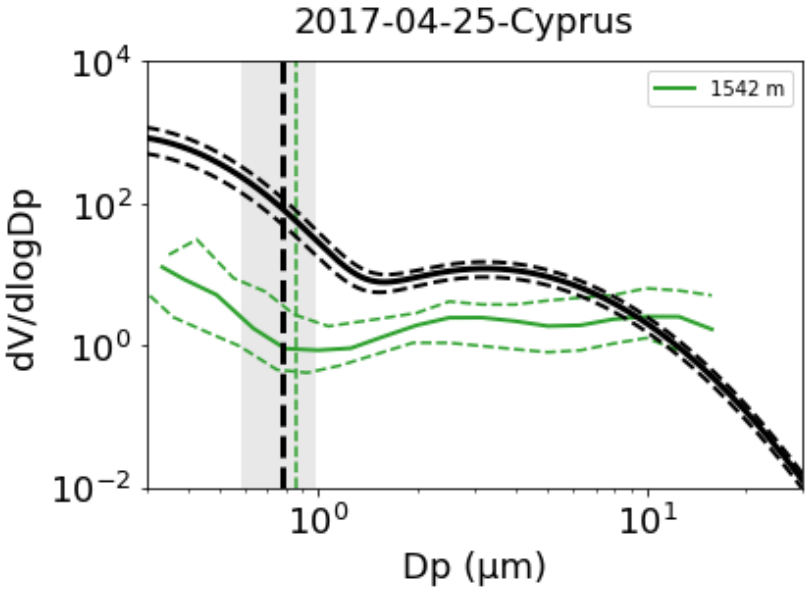

Figure 40 Case 9: Volume size distribution derived from lidar measurements (1.0 – 2.0 km height) using optimal estimation for aerosol type separation (black line, dashed lines indicate the uncertainty) compared to size distributions measured on board of Falcon at various height levels (coloured lines). The dashed vertical lines indicate the effective diameter, the shaded area the uncertainty of the effective diameter.

In general, a good agreement between the size distribution in the same height range was found. The fine mode is more pronounced in the lidar retrieval. The volume concentration in the size range of the 300 to 800 nm particles is overestimated by a factor of 10 to 1000 compared to the in-situ measurements. A further possible reason might be that the in-situ observations used in this study have a lower size limit of 300 nm in diameter. The particles smaller than 300 nm in diameter are measured in cabin with the UHSAS. These data are currently being analyzed. In the dust dominated cases, the largest particles (> 10 µm in diameter) are underestimated by the lidar retrieval by around one order of magnitude. All in all, this shifts the effective diameter of the lidar observations generally to lower values. On 6 April 2017 (case 1 and 2), no fine mode was found by the optimal estimation method and therefore the effective diameter is slightly

larger and compares well to the in-situ measurements. These are the very first comparisons. HETEAC was not meant to deliver complete size distributions. However, these first comparisons are promising. More comparisons to airborne in situ observations are desirable to strengthen the algorithm.

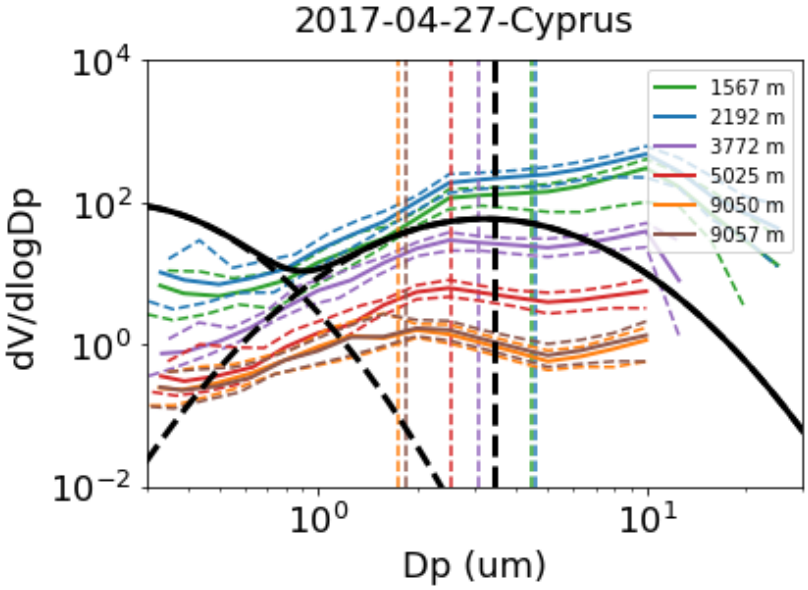

Figure 41 Case 10: Volume size distribution derived from lidar measurements (1.5 – 3.8 km height) using optimal estimation for aerosol type separation (black line, dashed lines for fine and coarse mode) compared to size distributions measured on board of Falcon at various height levels (coloured lines). The dashed vertical lines indicate the effective diameter. Optimal estimation results were not statistically significant within the 95% confidence interval. Therefore, no uncertainty estimates are provided.

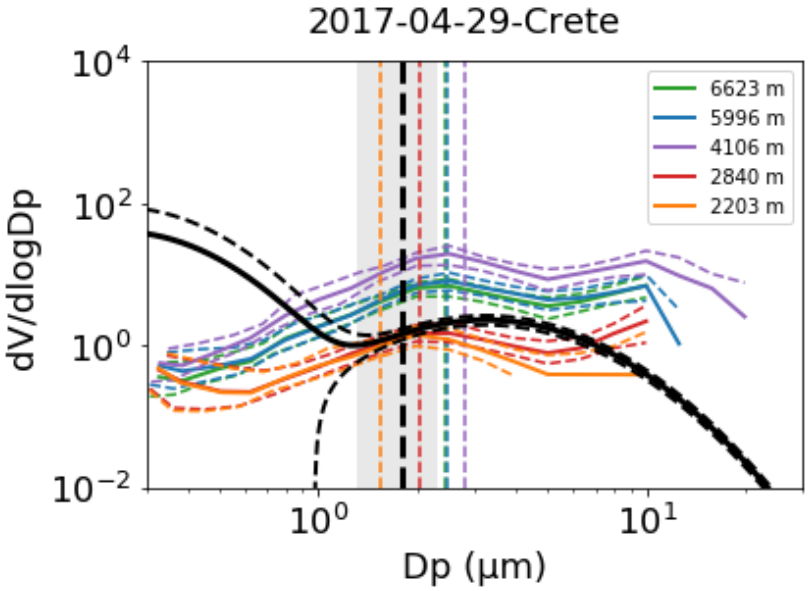

Figure 42 Case 11: Volume size distribution derived from lidar measurements (3.8 – 5.5 km height) using estimation for aerosol type separation (black line, dashed lines indicate the uncertainty) compared to size distributions measured on board of Falcon at various height levels (coloured lines). The dashed vertical lines indicate the effective diameter, the shaded area the uncertainty of the effective diameter.

5. SYNERGISTIC RADAR-LIDAR RETRIEVALS – DARDAR vs. CAPTIVATE

Besides the aerosol studies, the A-CARE project also included a comparative study of two synergistic radar-lidar retrievals of ice cloud properties. The DARDAR product (Delanoë and Hogan, 2010) is a well-established ice cloud product which combines joint observations from the Cloud Profiling Radar (CPR) on board CloudSat and from the Cloud-Aerosol Lidar with Orthogonal Polarization (CALIOP) on board CALIPSO. The synergistic product is derived using the optimal estimate algorithm VarCloud (Delanoë and Hogan, 2008). In this study, the operational setup (Version 2) described in Delanoë et al (2014) and the most recent advancements (Version 3) described in Cazenave et al (2019) are used. In anticipation of EarthCARE and building on the heritage of VarCloud, the CAPTIVATE retrieval is the second synergistic radar-lidar retrieval compared in this study. CAPTIVATE is outlined in Illingworth et al (2015) and currently in active development. The present study was only performed for ice cloud regions using the ESA release version 4.0.1 (DORSY VERSION exe: 4.01 proc: 4.02 format 4.20) with *atrain_atp_v1.cfg* as source configure file.

In a first step, the currently used microphysical assumptions and a priori profiles of DARDAR and CAPTIVATE were compared (Fig. 43). While DARDAR Version 2 relies on a combination of Brown and Francis (1995) and Mitchell et al (1996) to describe the relationship between the maximum diameter and the effective ice density of ice crystals (Fig. 43a), Version 3 is using the more recent in situ dataset of Heymsfield et al (2010). For ice clouds, CAPTIVATE (4.0.1) still relies on Brown and Francis (1995). Therefore, larger ice crystals are assumed to be less dense compared to DARDAR Version 3. A further difference is the semi-constant a priori profile of the normalized ice crystal number concentration N' of CAPTIVATE (Fig. 43c). At last, the a priori profiles and function to describe the lidar ratio S differ between both algorithms. While CAPTIVATE currently assumes a variable but constant lidar ratio throughout the atmosphere, ln(S) is assumed to vary linearly with temperature in DARDAR. Compared to Version 2, the temperature sensitivity of the lidar ratio model was reduced in Version 3 which leads to retrieved profiles of S which are more similar to CAPTIVATE.

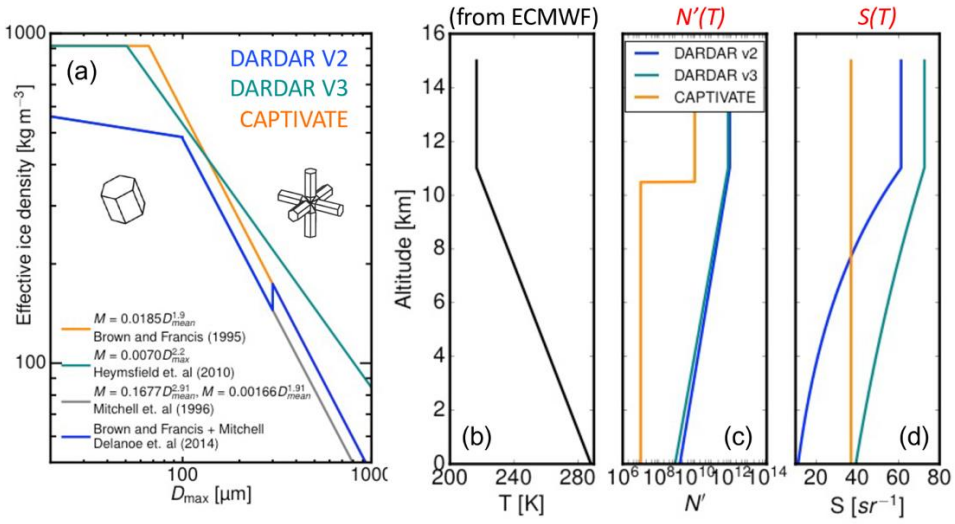

Figure 43 Comparison of microphysical assumptions and a priori profiles used in the optimal estimate products DARDAR (Version 2 / Version3) and CAPTIVATE to retrieve ice cloud microphysics from CALIPSO and CloudSat measurements. (a) Assumed mass-diameter relationship to model the decreasing effective ice density of larger ice crystals, (b) Both algorithms use the temperature profile from ECMWF to start the optimal estimate with different (c) a-priori profiles of the normalized ice crystal number concentration and (d) a-priori profiles of the lidar ratio.

A further difference exists between the assumed particle size distribution. CAPTIVATE relies on the modified Gamma size distribution (with shape parameter μ = 2) to reduce the natural variability of ice particle sizes into a mean particle size (Fig. 44a), while DARDAR is based on a normalized size distribution (Fig. 44b, c) described in Delanoë et al (2014) and updated by Cazenave (2019). Preparatory studies have shown that the different relationships between the maximum diameter and the effective ice density of ice crystals are dominating the differences between the retrieval results, while the different particle size distributions play only a minor role.

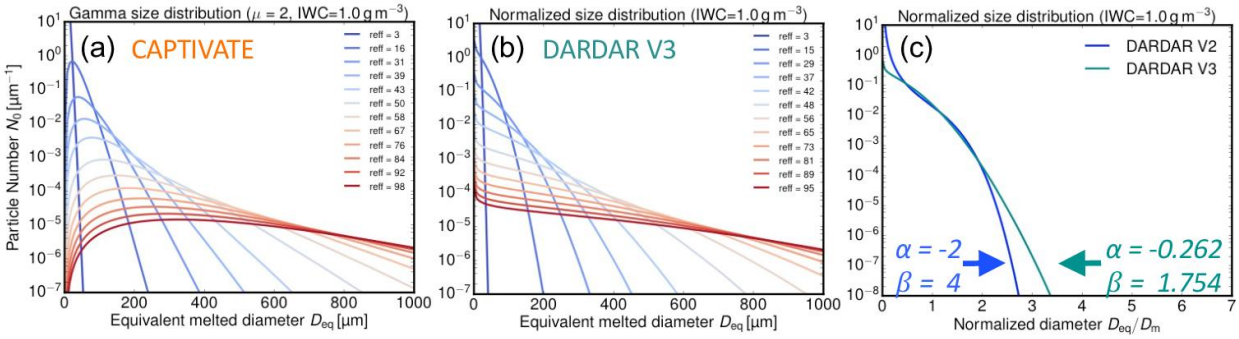

Figure 44 Comparison of particle size assumptions for different effective radii (blue to red curves) used in the optimal estimate algorithms DARDAR (Version 2 / Version3) and CAPTIVATE to retrieve ice cloud microphysics from CALIPSO and CloudSat measurements. While the (a) modified Gamma size distribution is used by the CAPTIVATE algorithm, the (b) DARDAR algorithm uses the normalized size distribution following Delanoë et al (2014). In (c) the updated particle size distribution used in Version 3 following Cazenave et al (2019) is compared against the currently used parameterization in Version 2.

To compare the performance of both algorithms, the same example case of A-Train measurements taken on the 2nd January 2007 between 16:27 – 16:29 UTC was used as input (Fig. 45). To separate the influence of the different implementations of the optimal estimation from the different microphysical assumptions, DARDAR Version 2 was compared to the current version of CAPTIVATE (Fig. 46). Subsequently, the CAPTIVATE setup parameters were changed to reflect the microphysical assumptions of DARDAR Version 3 (Fig. 47).

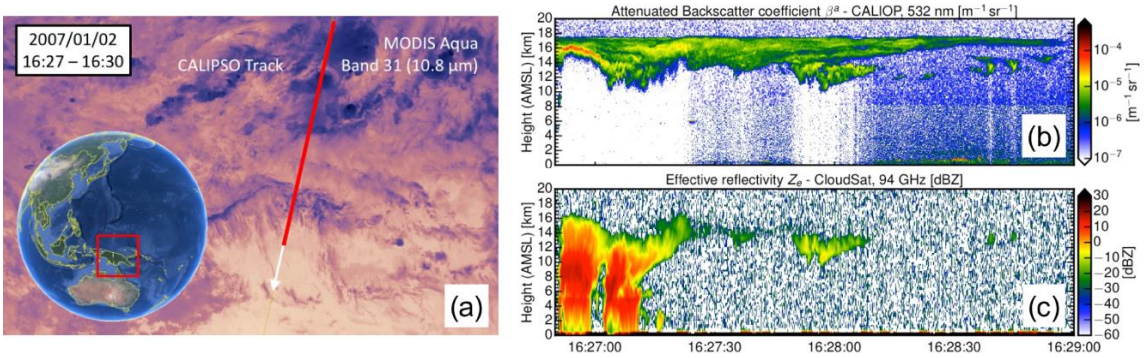

Figure 45 Example case of A-Train measurements on the 2nd January 2007 between 16:27 – 16:29 UTC used for the algorithm comparison. (a) MODIS Band 31 (10.8 µm) satellite picture with CALIPSO/CloudSat overpass (red line), (b) CALIPSO attenuated backscatter coefficient at 532 nm and (c) CloudSat effective reflectivity at 94 GHz.

In Fig. 46, the ice cloud microphysics retrieved by VarCloud with the DARDAR Version 2 microphysics is shown in the left panels, while the retrieval results with the current CAPTIVATE assumptions is shown in the right panels. While the retrieved extinction (Fig. 46a, e) and ice water content (Fig. 46b, f) are quite similar for the two different algorithms, larger differences become apparent between the retrieved effective radius of ice crystals (Fig. c, g). This can be explained by the strongly different lidar ratios (Fig. 46 d, h), where

CAPTIVATE uses a constant value throughout a profile while DARDAR Version 2 show unrealistic high lidar ratios and thus very small effective radii at cloud tops. This deficiency was recently addressed in Cazenave et al (2019) and corrected in DARDAR Version 3. In the absence of CloudSat measurements (at thinner cirrus regions), the constant lidar ratio of CAPTIVATE leads to apparent jumps of the effective radii between adjacent profiles (Fig. 46g).

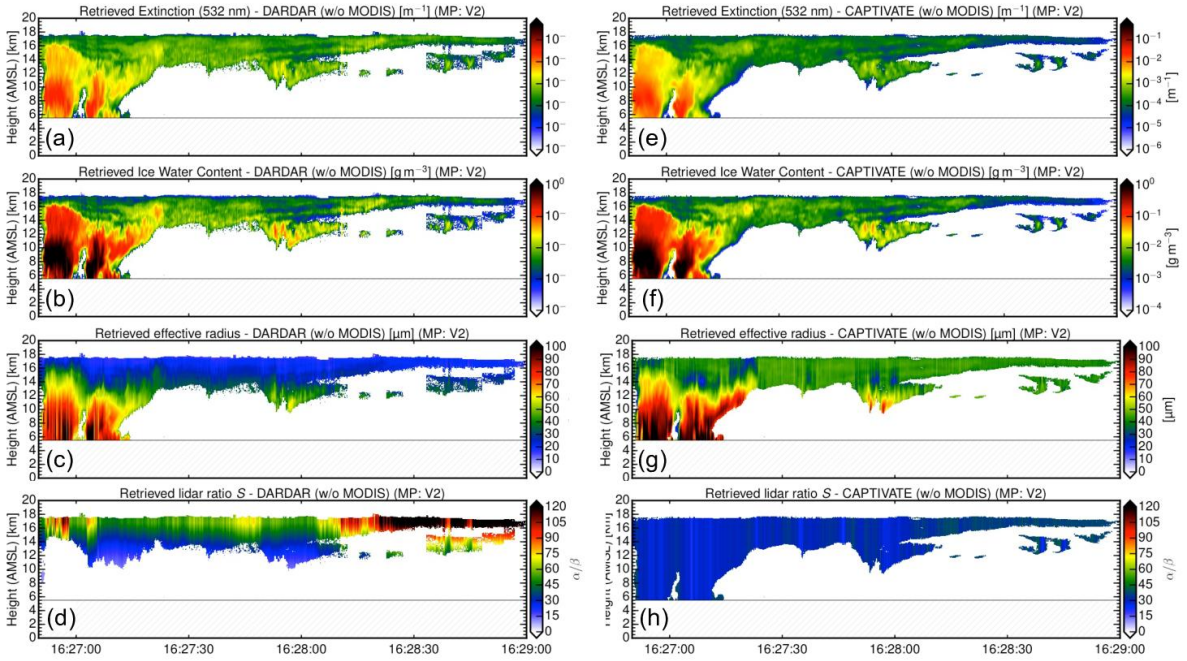

Figure 46 Comparison of retrieved ice cloud microphysics derived by the DARDAR algorithm Version 2 (left panels) and the CAPTIVATE algorithm (right panels) with their current microphysical assumptions. While (a, e) the retrieved extinction and (b, f) and the retrieve ice water content are quite similar between the algorithms, larger differences become apparent between (c, g) the retrieved effective radius of ice crystals due to different (d, h) different lidar ratios.

With a more moderate temperature sensitivity of the lidar ratio in Version 3 of DARDAR, the retrieved effective radius is in better agreement with CAPTIVATE. This becomes apparent in Fig. 47 which compares the retrieved ice water content (left panels) and effective radius of ice crystals (right panels) between DARDAR and CAPTIVATE. Here, the top panels compare the retrieval results for the old microphysical assumptions, the bottom panels for the new assumptions with the updated lidar ratio. While the effective radii now show a better agreement between both algorithms in Fig. 47d), a larger disagreement at higher ice water contents becomes apparent in Fig. 47c). This can be attributed to the different mass-diameter relationships mentioned earlier where CAPTIVATE still uses the less dense ice crystals of Brown and Francis (1995).

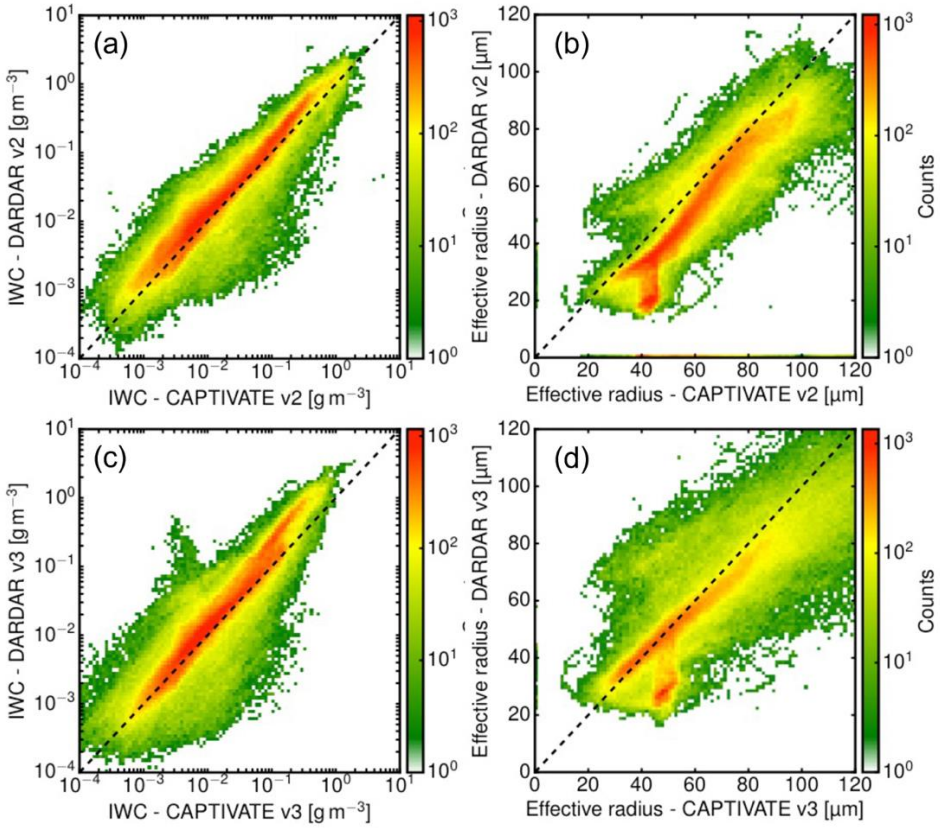

Figure 47 Comparison of (a) retrieved ice water content and (b) effective radius of ice crystals between DARDAR and CAPTIVATE with their current microphysics assumptions. The same comparison of (c) retrieved ice water content and (d) effective radius of ice crystals between DARDAR and CAPTIVATE with Version 3 microphysics.

6. SUMMARY AND CONCLUSION

The A-CARE project offered the unique possibility to do the first validations of the aerosol type separation algorithm and the prescribed microphysics. 11 cases, 8 close to Limassol, Cyprus, 3 close to Finokalia, Crete, have been selected to cover a wide range of aerosol types from rather pure dust (case 10), to dusty mixtures (case 1, 2 & 6) and polluted conditions (case 4) and marine influence (case 5 & 11), nicely summarized in Figure 32.

The direct comparison to airborne in situ measurements has shown that the microphysical assumptions are valid and that even complex aerosol mixtures, e.g., case 9 (25 April 2017), could be separated into individual aerosol components in a satisfying manner. A future step would be to compare the refractive index retrieved from the lidar observations to the particle collected on filters during the flights. These filter probes are currently analysed by the Technical University of Darmstadt in the group of Konrad Kandler.

The test with real world data has led to a revision of the EarthCARE aerosol classification schemes. The assumptions used for HETEAC compare well to the airborne in situ observations. A further classification scheme implemented in the ATLID-MSI synergy processor AM-COL have turned out to be less useful, as it is only based on aerosol optical thickness (AOT) and the Ångström exponent between 355 and 670 nm. It is under consideration to remove this scheme from the L2 algorithms and replace it by a better combination of ATLID optical properties on the track extended to the MSI swath.

5 ACKNOWLEDGEMENT

6 REFERENCES

Brown, P. R. A., & Francis, P. N.: Improved Measurements of the Ice Water Content in Cirrus Using a Total-Water Probe, *Journal of Atmospheric and Oceanic Technology*, *12*(2), 410-414, 1995.

Cazenave, Q., Ceccaldi, M., Delanoë, J., Pelon, J., Groß, S., and Heymsfield, A.: Evolution of DARDAR-CLOUD ice cloud retrievals: new parameters and impacts on the retrieved microphysical properties, Atmos. Meas. Tech., 12, 2819–2835, 2019.

Delanoë, J., and Hogan, R. J.: A variational scheme for retrieving ice cloud properties from combined radar, lidar, and infrared radiometer, *J. Geophys. Res.*, 113, D07204, 2008.

Delanoë, J., and Hogan, R. J.: Combined CloudSat-CALIPSO-MODIS retrievals of the properties of ice clouds, *J. Geophys. Res.*, 115, D00H29, 2010.

Delanoë, J. M. E., Heymsfield, A. J., Protat, A., Bansemer, A., and Hogan, R. J.: Normalized particle size distribution for remote sensing application, *J. Geophys. Res. Atmos.*, 119, 4204–4227, 2014.

Engelmann, R., Kanitz, T., Baars, H., Heese, B., Althausen, D., Skupin, A., Wandinger, U., Komppula, M., Stachlewska, I. S., Amiridis, V., Marinou, E., Mattis, I., Linné, H., and Ansmann, A.: The automated multiwavelength Raman polarization and water-vapor lidar PollyXT: the neXT generation, Atmos. Meas. Tech., 9, 1767–1784, https://doi.org/10.5194/amt-9-1767-2016, 2016.

Heymsfield, A. J., Schmitt, C., Bansemer, A., & Twohy, C. H.: Improved Representation of Ice Particle Masses Based on Observations in Natural Clouds, *Journal of the Atmospheric Sciences*, *67*(10), 3303-3318, 2010.

Illingworth, A. J., Barker, H. W., Beljaars, A., Ceccaldi, M., Chepfer, H., Clerbaux, N., Cole, J., Delanoë, J., Domenech, C., Donovan, D. P., Fukuda, S., Hirakata, M., Hogan, R. J., Huenerbein, A., Kollias, P., Kubota, T., Nakajima, T., Nakajima, T. Y., Nishizawa, T., Ohno, Y., Okamoto, H., Oki, R., Sato, K., Satoh, M., Shephard, M. W., Velázquez-Blázquez, A., Wandinger, U., Wehr, T., & van Zadelhoff, G.-J.: The EarthCARE Satellite: The Next Step Forward in Global Measurements of Clouds, Aerosols, Precipitation, and Radiation, *Bulletin of the American Meteorological Society*, *96*(8), 1311-1332, 2015.

Janjic, Z. I., Gerrity Jr., J. P., and Nickovic, S.: An Alternative Approach to Nonhydrostatic Modeling, Mon. Weather Rev., 129, 1164–1178, 2001.

Mitchell, D. L.: Use of Mass- and Area-Dimensional Power Laws for Determining Precipitation Particle Terminal Velocities, *Journal of Atmospheric Sciences*, *53*(12), 1710-1723, 1996.

Nickovic S., A. Papadopoulos, O. Kakaliagou and G. Kallos, Model for prediction of desert dust cycle in the atmosphere. J. Geophys. Res., 106, 18113-18129., 2001.

Stohl, A.; Forster, C.; Frank, A.; Seibert, P.; Wotawa, G. Technical note: The Lagrangian particle dispersion model FLEXPART version 6.2. Atmos. Chem. Phys., 5, 2461–2474, 2005.
Wandinger et al., HETEAC: The Aerosol Classification Model for EarthCARE, EPJ Web of Conferences, 119, 01004, 2016.

Annex 1: DATA ACQUISITION REPORT (DAR)